



Direct numerical simulations of compressible turbulent channel flows with asymmetric thermal walls

Peng Zhang¹, Yubin Song² and Zhenhua Xia^{2,†}

¹College of Metrology and Measurement Engineering, China Jiliang University, Hangzhou 310018, PR China

²State Key Laboratory of Fluid Power and Mechatronic Systems and Department of Engineering Mechanics, Zhejiang University, Hangzhou 310027, PR China

(Received 5 October 2023; revised 24 February 2024; accepted 1 March 2024)

This paper extends the work of Tamano & Morinishi (*J. Fluid Mech.*, vol. 548, 2006, pp. 361–373) by simulating supersonic turbulent channel flow with asymmetric thermal walls using a larger computational domain and a finer mesh. Direct numerical simulation is carried out for four cases with different thermal wall boundaries at the top wall at fixed $Ma = 1.5$, $Re = 6000$ and $Pr = 0.72$, while the bottom wall is maintained at a constant temperature of T_L equal to the reference temperature. These cases are referred to as the adiabatic case TAd, where the top wall is adiabatic; the pseudo-adiabatic case T32, where the top wall is isothermal with temperature $T_{w,t} = T_A$; the sub-adiabatic case T25, with $T_{w,t} = 0.77T_A$; and the super-adiabatic case T40, with $T_{w,t} = 1.24T_A$. Here, $T_A = 3.234$ is the mean temperature at the adiabatic wall in the TAd case. The objective of this study is to compare and contrast the TAd case with its corresponding T32 case, and to investigate the effect of the wall temperature difference between the two isothermal walls. Comparisons of the basic turbulent statistics, the heat transfer between the Favre-averaged mean-flow kinetic energy, the Favre-averaged turbulent kinetic energy and the Favre-averaged mean internal energy, as well as the wall heat transfer properties, indicate that the TAd case and its corresponding T32 case are generally equivalent. The only discernible difference is in the region very close to the top wall for the temperature-fluctuation-related quantities. The analysis reveals that the asymmetry of the thermal walls causes asymmetry in the flow and thermal fields. In addition, the transfer of the heat generated by the pressure dilatation and the viscous stress is facilitated by the turbulent heat flux term and the mean molecular heat flux term.

Key words: compressible turbulence, turbulence simulation, supersonic flow

† Email address for correspondence: xiazh1006@163.com

1. Introduction

The investigation of compressible wall-bounded turbulence has always been an important topic and is widely relevant in the aerospace industry. The majority of the early experimental studies have been reviewed by Spina, Smits & Robinson (1994), Bradshaw (1977) and Gatski & Bonnet (2013). Compared with incompressible wall-bounded turbulence, the compressibility effect has become one of the critical issues, and different Mach numbers and thermal wall boundaries will affect the compressibility of the flow. Morkovin (1962) first hypothesized that if density fluctuations are small relative to the mean density, their effect on turbulence is small and can be ignored. This hypothesis is known as Morkovin's hypothesis, and it has led to several compressibility transformations for velocity and Reynolds stresses that aim to map the compressible turbulent statistics onto the 'equivalent' incompressible ones using the mean profiles of density and viscosity (Van Driest 1951; Huang, Coleman & Bradshaw 1995; Trettel & Larsson 2016; Volpiani *et al.* 2020; Griffin, Fu & Moin 2021; Hasan *et al.* 2023).

As one of the canonical flow problems in compressible wall-bounded turbulence, compressible turbulent channel flows with symmetric isothermal walls have been much studied in past decades since the pioneering work by Coleman, Kim & Moser (1995), who performed direct numerical simulations (DNS) of supersonic turbulent channel flows at Mach number (Ma) 1.5 and 3.0. Here, Ma is based on the bulk velocity and sound speed at the wall. They reported that isothermal boundary conditions led to flow that is strongly influenced by wall-normal gradients of mean density and temperature, and these gradients enhanced the streamwise coherence of the near-wall streaks, while almost supporting Morkovin's hypothesis. That is, the turbulent statistics at both Mach numbers agreed well with the corresponding incompressible cases when they were properly scaled. Huang *et al.* (1995) further analysed the above DNS data, and confirmed that the compressibility effects due to the turbulent density and pressure fluctuations were insignificant. They also found that the strong Reynolds analogy was invalid according to the DNS data, and proposed a more general representation of the analogy. Compressible turbulent channel flows with symmetric isothermal walls were also studied by Foysi, Sarkar & Friedrich (2004), Wei & Pollard (2011), Modesti & Pirozzoli (2016), Gerolymos & Vallet (2023), Yu, Xu & Pirozzoli (2019), Tang *et al.* (2020), Zhang & Xia (2020), Baranwal, Donzis & Bowersox (2022), Cheng, Shyy & Fu (2023) and Cheng & Fu (2023). Recently, Yao & Hussain (2020) carried out a series of DNS of this problem, where $Ma = 0.8$ and 1.5, and the bulk Reynolds number Re was in the range of 3000–34 000. They confirmed that the mean velocity profiles, as well as the Reynolds stress profiles, perfectly collapsed to their corresponding incompressible profiles after the Trettel and Larsson (TL) transformation (Trettel & Larsson 2016). Furthermore, their results revealed that the typical eddy size did not vary with Ma when scaled using the local friction velocity and thermodynamic properties, and that the compressibility contribution to the skin friction continuously decreases with Re , suggesting that compressible and incompressible flows differ little when Re is high enough. Song *et al.* (2022) proposed a semi-empirical scaling for the central mean temperature based on the generalized Reynolds analogy (Zhang *et al.* 2014) and available DNS data. Using this empirical scaling, Song, Zhang & Xia (2023) proposed a robust iterative method to obtain the mean profiles at given Ma and Re in compressible turbulent channel flows without performing DNS. More recently, Gerolymos & Vallet (2024) performed DNS of compressible turbulent channel flows with symmetric isothermal cold walls across a range of centreline Mach numbers and Reynolds numbers. That study focused on the statistics of the total and static temperature (and enthalpy). The results indicated that the streamwise velocity fluctuations correlate strongly

with the total enthalpy fluctuations, while they are not well correlated with the static enthalpy.

In addition to the symmetric isothermal cases, the two walls in compressible turbulent channel flows can also be thermodynamically asymmetric, and understanding the effects of this asymmetry is important to complement the former studies. In general, there are two possible scenarios. One is the case of a temperature difference between two isothermal walls, and the other is the case of an isothermal wall and an adiabatic wall, or the case of isothermal–adiabatic (I–A) walls. The first case has been studied by several groups using DNS or large-eddy simulations, and most of them have focused on the nearly incompressible situations (Wang & Pletcher 1996; Lessani & Papalexandris 2008; Nagata & Nagaoka 2017; Ma, Yang & Ihme 2018; Avellaneda *et al.* 2021), which are believed to be closely related to the flow characteristics in solar receivers (Serra *et al.* 2012; Avellaneda, Bataille & Toutant 2019; Toki, Teramoto & Okamoto 2020). For the fully compressible situations with $Ma > 0.3$, studies are rather scarce, and they were carried out mainly to serve as a comparison object for the latter I–A cases (Tamano & Morinishi 2006; Baranwal, Donzis & Bowersox 2023).

In fact, compressible I–A channel flows were first used as a validation case for the B-spline collocation method by Morinishi, Tamano & Nakabayashi (2003). Later on, Morinishi, Tamano & Nakabayashi (2004) carried out a thorough investigation of the effects of adiabatic and isothermal conditions on the turbulent statistics in a compressible I–A channel at $Ma = 1.5$. They reported that Morkovin’s hypothesis was not applicable to the near-wall asymptotic behaviour of the wall-normal turbulence intensity, even when the variable property effect was considered. Furthermore, they identified the difference between the energy transfer near isothermal and adiabatic walls by comparing the internal energy and the mean and turbulent kinetic energies.

Tamano & Morinishi (2006) extended the work of Morinishi *et al.* (2004), aiming to clarify the effect of thermal wall boundary conditions on turbulence statistics and structures in compressible turbulent channel flows, and to address whether the variations of turbulence statistics are attributable to the effect of the increase in wall temperature caused by the adiabatic wall boundary condition. They simulated a ‘corresponding’ isothermal–pseudo-adiabatic (I–PA) case, where the wall temperature of the upper wall was set to the mean wall temperature of the adiabatic wall, keeping all the other flow parameters the same as those in the I–A case. They reported that the thermal statistics in the I–A case were quite different from those in the corresponding I–PA case. More specifically, they reported that the profiles of mean temperature and root-mean-square (r.m.s.) temperature fluctuations between the I–PA and I–A cases were obviously different, with near-wall maximums appearing near the high-temperature wall for the two profiles in the I–PA case, and that the direction of energy transfer due to pressure work near the adiabatic wall being opposite to that near the isothermal wall is attributable to the effect of the high-temperature wall, not to the effect of the adiabatic wall. However, a subsequent study by Shadloo, Hadjadj & Hussain (2015) demonstrated that the basic turbulent statistics in supersonic boundary layers remain unaffected by the thermal boundary conditions between a real adiabatic wall and the corresponding pseudo-adiabatic wall. Zhang *et al.* (2022) demonstrated that the deviations caused by the three ‘equivalent’ canonical thermal boundary conditions in compressible turbulent channel flows – namely the first boundary condition with fixed wall temperature, the second boundary condition with fixed wall heat flux and the third mixed boundary condition – are limited to the near-wall region. The statistical differences between the I–A case and its corresponding

I–PA case from Tamano & Morinishi (2006) contradict the conclusions drawn by Shadloo *et al.* (2015) and Zhang *et al.* (2022), which suggested that the cases were nearly equivalent. Therefore, it is necessary to conduct a thorough investigation of the similarities and differences between the two cases.

It is noteworthy that the compressible I–A channel has recently attracted attention. Lusher & Coleman (2022a,b) conducted DNS of turbulent I–A channels at various Mach and Reynolds numbers to investigate the effect of thermal wall conditions on the turbulent Prandtl number (Pr_t) in the low-supersonic regime. They believed that the adiabatic condition was a new feature of particular interest. It was found that Pr_t approaches 0.85 away from both the isothermal and the adiabatic walls. The near-wall variations of Pr_t collapse as a function of the semi-local wall scaling proposed by Huang *et al.* (1995), showing only a weak dependence on the wall-friction Reynolds number. Huang *et al.* (2023) further investigated the velocity and temperature scaling near isothermal and adiabatic walls using the data from Lusher & Coleman (2022a). Baranwal *et al.* (2023) performed a series of DNS to study the near-wall asymptotic behaviour for the compressible I–A and I–PA cases. That study complemented their earlier research on symmetric isothermal channels (Baranwal *et al.* 2022). The researchers believed that adiabatic walls could isolate the effects of Mach number from wall cooling, providing a more direct way to assess the effects of Mach number and the validity of Morkovin’s hypothesis on the asymptotic scaling of turbulent statistics.

This paper studies supersonic turbulent channel flows with asymmetric thermal walls. The study includes one I–A case and its corresponding I–PA case, as well as two cases with asymmetric isothermal walls of different wall temperature differences. The aim of this study is to clarify the similarities and differences between the I–A case and its corresponding I–PA case, using reliable DNS data to carefully address the conflicts mentioned above. Additionally, we investigate the effect of wall temperature differences between two isothermal walls, especially on the heat transfer behaviour of the channel system with asymmetric wall conditions. The paper is organized as follows. The physical model and numerical set-up are described in § 2. Some basic turbulence statistics are given in § 3. The energy exchange and heat transfer properties are studied in §§ 4 and 5, respectively. Finally, some conclusions are drawn in § 6.

2. Problem description and numerical set-up

In this paper, our main concern is compressible turbulent channel flows between two walls, as depicted in figure 1. The bottom wall is isothermal with fixed wall temperature T_L , whereas the top wall is either adiabatic or isothermal with fixed wall temperature $T_{w,t}$. The flow is driven by a uniform force in the streamwise direction. Here, x , y and z denote the streamwise, wall-normal and spanwise directions, respectively; x_1 , x_2 and x_3 are used interchangeably with x , y and z . The governing equations are the compressible Navier–Stokes equations, which can be rewritten as follows:

$$\frac{\partial \rho}{\partial t} + \frac{\partial \rho u_j}{\partial x_j} = 0, \tag{2.1}$$

$$\frac{\partial \rho u_i}{\partial t} + \frac{\partial \rho u_i u_j}{\partial x_j} = -\frac{\partial p}{\partial x_i} + \frac{\partial \tau_{ij}}{\partial x_j} + f_i \delta_{i1}, \tag{2.2}$$

$$\frac{\partial E}{\partial t} + \frac{\partial [u_i(E + p)]}{\partial x_i} = -\frac{\partial q_j}{\partial x_j} + \frac{\partial u_i \tau_{ij}}{\partial x_j} + f_1 u_1. \tag{2.3}$$

DNS of compressible turbulent channel flows

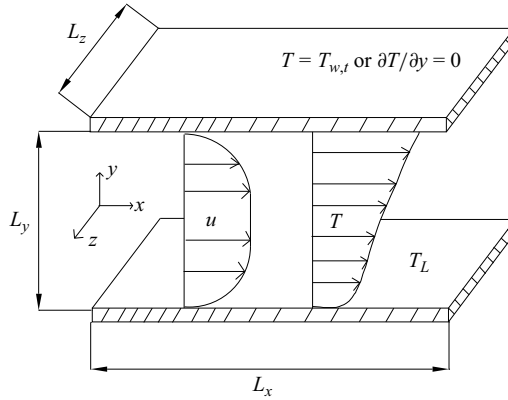


Figure 1. Sketch of compressible turbulent channel flows. The bottom wall is isothermal with $T_w = T_L$, whereas the top wall is either adiabatic ($\partial T/\partial y = 0$) or isothermal with wall temperature $T_{w,t}$.

Here, the Einstein summation convention and notation are used; δ_{ij} is the Kronecker tensor, ρ the fluid density, u_i the i th component of the velocity, p the pressure, f_i the driving volume force and $E = \rho(e + u_i^2/2)$ the total energy. In the present study, the fluid is assumed to be a perfect gas, and the equation of state $p = \rho RT$ is used, where R and T are the gas constant and temperature, respectively. Here, $e = C_v T$ is the internal energy, with $C_v = R/(\gamma - 1)$ being the specific heat at constant volume, and $\gamma = C_p/C_v$ is the specific heat ratio, with C_p being the specific heat at constant pressure. The viscous stress τ_{ij} and heat flux q_j are given as

$$\tau_{ij} = \mu \left(\frac{\partial u_i}{\partial x_j} + \frac{\partial u_j}{\partial x_i} - \frac{2}{3} \frac{\partial u_k}{\partial x_k} \delta_{ij} \right), \quad q_j = -\lambda \frac{\partial T}{\partial x_j}, \quad (2.4a,b)$$

where μ , the molecular viscosity, obeys the Sutherland formula and λ , the thermal conductivity, is related to μ through the Prandtl number $Pr = C_p \mu / \lambda = 0.72$. In what follows, all quantities are non-dimensionalized by the reference temperature $T_{ref} = 288.15$ K, the channel half-width h , the bulk density $\rho_m = \int_{-h}^h \bar{\rho} dy / (2h)$ and the bulk velocity $u_m = \int_{-h}^h \bar{\rho} u dy / (2h \rho_m)$ (where $\bar{(\cdot)}$ denotes the Reynolds-averaging operation in the homogeneous directions and time) unless stated otherwise. Besides Pr , the other two controlling (input) parameters, i.e. the Reynolds number and Mach number,

$$Re = \frac{\rho_m u_m h}{\mu_{ref}} = 6000, \quad Ma = \frac{u_m}{\sqrt{\gamma R T_{ref}}} = 1.5, \quad (2.5a,b)$$

are also fixed unless otherwise stated. Here, μ_{ref} is the viscosity at the reference temperature T_{ref} .

In the present study, the simulations are carried out by using the OPENCFD-SC code on a computational box of size $L_x \times L_y \times L_z = 6\pi \times 2 \times 4\pi/3$. In the OPENCFD-SC code, the inviscid and viscous terms are discretized using a seventh-order upwind scheme and an eighth-order central scheme, respectively, and time is advanced using an explicit third-order Runge–Kutta scheme. The OPENCFD-SC code has been widely employed and validated for compressible turbulent boundary layers (Zhang *et al.* 2014; Liang & Li 2015; Li *et al.* 2019b; Xu *et al.* 2021) and plane channel flows (Chen & Fei 2018; Yu *et al.* 2019; Zhang & Xia 2020). The flow is assumed to be periodic in the streamwise and spanwise

Case	Thermal condition (top)	T_L/T_{ref}	$N_x \times N_y \times N_z$	$T_{w,t}/T_L$	N_t	Line style
TAd	$\partial T/\partial y = 0$	1.0	$864 \times 240 \times 320$	3.234	387	—
T32	$T_{w,t}/T_{ref} = 3.234$	1.0	$864 \times 240 \times 320$	3.234	355	+++
T25	$T_{w,t}/T_{ref} = 2.5$	1.0	$864 \times 240 \times 320$	2.5	378	---
T40	$T_{w,t}/T_{ref} = 4.0$	1.0	$864 \times 240 \times 320$	4.0	393	-. -. -

Table 1. Control parameters and numerical set-up. In all cases, $Ma = 1.5$, $Re = 6000$, $Pr = 0.72$ and $\gamma = 1.4$. The computational domain is $L_x \times L_y \times L_z = 6\pi \times 2 \times 4\pi/3$. The temperatures T_{ref} , T_L and $T_{w,t}$ are the reference temperature, the wall temperature at the bottom wall and the mean temperature at the top wall, respectively. The parameter N_t is the number of samples used in the statistics with time interval $\Delta t = 0.8h/u_m$. The line styles for the four cases are used unless otherwise stated.

Case	Re_τ	Re_τ^*	Δx^+	Δy_{min}^+	Δy_{max}^+	Δz^+	Re_τ	Re_τ^*	Δx^+	Δy_{min}^+	Δy_{max}^+	Δz^+
TAd	585	205	12.76	0.73	10.15	7.65	135	192	2.94	0.17	2.34	1.76
T32	584	205	12.74	0.73	10.13	7.65	135	192	2.94	0.17	2.34	1.76
T25	537	219	11.71	0.67	9.32	7.02	169	211	3.68	0.21	2.93	2.21
T40	631	192	13.76	0.79	10.95	8.25	115	179	2.51	0.14	2.00	1.50

Table 2. Grid resolutions. Here $Re_\tau = \rho_w u_\tau h / \mu_w$ is the friction Reynolds numbers defined using the quantities at the nearest wall, while $Re_\tau^* = \bar{\rho}_c (\tau_w / \bar{\rho}_c)^{1/2} h / \bar{\mu}_c$ is the friction Reynolds number based on the centreline density and viscosity and the friction at the wall; Δx and Δz are the grid spaces in the streamwise and spanwise directions; Δy_{min} and Δy_{max} denote the wall-normal grid spaces near the wall and at the channel centre. Columns 2–7 display the results normalized by the quantities at the bottom wall ($y = -1$), and columns 8–13 show the results at the top wall ($y = 1$).

directions. The boundary conditions for the velocity at both walls are no-slip, whereas the thermal boundaries are different, as mentioned above. The specific control parameters are shown in [table 1](#). The grid is uniform in the streamwise and spanwise directions, and it is clustered in the near-wall region in the wall-normal direction. The detailed grid resolutions are shown in [table 2](#), where the superscript ‘+’ denotes normalization by using the viscous scale δ_v at the nearest wall (also referred to as the wall coordinate). Here, $\delta_v = \mu_w / (\rho_w u_\tau)$ and $u_\tau = (|\tau_w| / \rho_w)^{1/2}$ with μ_w , ρ_w and τ_w being the viscosity, density and wall shear stress at the nearest wall, respectively. It is found that the current resolutions are comparable to those used by Yao & Hussain (2020), Lusher & Coleman (2022a) and Gerolymos & Vallet (2023). [Figure 2](#) displays the ratio between the local wall-normal resolution Δy and the local Kolmogorov scale η_k in the wall-normal direction for the cases TAd, T25 and T40, demonstrating the sufficiency of the present grid resolutions. Here, $\eta_k = (\bar{\rho} \nu^3 / \varepsilon_k)^{1/4}$, with $\nu = \bar{\mu} / \bar{\rho}$ being the mean local kinematic viscosity and ε_k the dissipation rate of turbulent kinetic energy (see (4.3) later). It is evident from [figure 2\(a\)](#) that $\Delta y / \eta_k$ is less than 1.15 across the channel for the three cases TAd, T25 and T40, indicating that the present mesh resolutions meet the requirement stated by Moin & Mahesh (1998) that the smallest resolved length scale should be $O(\eta_k)$. Near the bottom isothermal wall, $\Delta z^+ \approx 7-8$, which may be considered slightly coarse for the current simulations. However, as shown in [figure 2\(b\)](#), $\Delta z / \delta_v^*$ (see the definition of δ_v^* later) decays rapidly near the bottom wall and remains below 4 for most of the channel ($y > -0.9$). We have also refined the grid resolution in the wall-normal and spanwise directions, as well as in the streamwise direction for the TAd case. The results, presented in the [Appendix](#), further confirm the adequacy of the current grid resolutions.

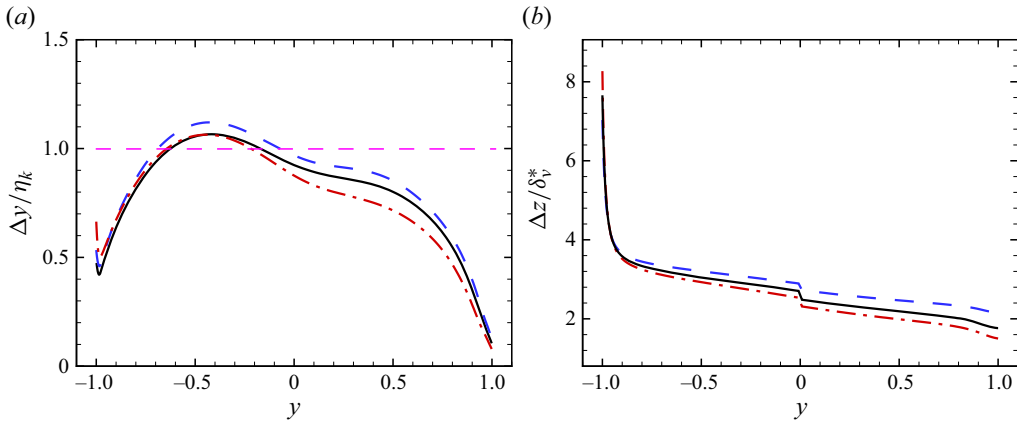


Figure 2. (a) The ratio between the local wall-normal resolution Δy and the local Kolmogorov scale η_k and (b) the ratio between the spanwise resolution Δz and the semi-local viscous length scale δ_v^* in the wall-normal direction for TAd, T25 and T40. The line styles of the cases are as presented in table 1.

The initial velocity fields in the present cases are the laminar parabolic one superimposed with random disturbances, while the density and temperature are uniform. The simulations were initially run on a very coarse mesh and then interpolated to the target fine mesh. Each case was executed using 480 CPU processes for over $400h/u_m$ until the flows reached a stationary state. At this point, the turbulent statistics, such as the friction Reynolds numbers at the bottom and top walls, oscillated within a certain range. Then N_t samples of the flow fields were stored with a time interval of $\Delta t = 0.8h/u_m$ for statistical analysis. In the Appendix, a convergence study was conducted, and it was found that most results converged with 100 samples.

In the following, Reynolds decomposition ($\phi = \bar{\phi} + \phi'$ with $\bar{\phi} = \langle \phi \rangle$) and density-weighted Favre decomposition ($\phi = \tilde{\phi} + \phi''$ with $\tilde{\phi} = \overline{\rho\phi}/\bar{\rho}$ and $\tilde{\phi} = \{\phi\}$) are used, where $\langle \phi \rangle = \bar{\phi}$ denotes the averaging operator in the homogeneous spatial directions (x and z) and the temporal direction (t) by using the N_t samples of the flow fields. Correspondingly, the r.m.s. value can be defined as $\phi_{rms} = (\overline{\phi'^2})^{1/2}$. Furthermore, besides the global coordinate, where y is normalized by h , and the wall coordinate, the semi-local coordinate is also used, where y is normalized by the semi-local viscous length scale $\delta_v^* = \bar{\mu}(y)/(\bar{\rho}(y)u_\tau^*)$ with $u_\tau^* = (|\tau_w|/\bar{\rho}(y))^{1/2}$ being the semi-local friction velocity. It is obvious that variations of mean density and mean viscosity in the wall-normal direction affect the semi-local coordinate, and its effectiveness has been well documented by many authors (Huang *et al.* 1995; Morinishi *et al.* 2004; Modesti & Pirozzoli 2016). Similarly, the friction temperature and the semi-local friction temperature can be defined as $T_\tau = q_w/(C_p\rho_w u_\tau)$ and $T_\tau^* = q_w/(C_p\bar{\rho}(y)u_\tau^*)$, respectively. It is important to note that $q_w = 0$ and $q_w \approx 0$ for the adiabatic and pseudo-adiabatic walls, respectively. Therefore, T_τ and T_τ^* are not applicable.

3. Basic turbulence statistics

In compressible turbulence, the velocity and temperature fields are coupled. In turbulent channel flows, it is intuitively expected that the asymmetry of the thermal boundary condition at the two walls will change the symmetry properties of the mean temperature, mean density and mean streamwise velocity. Figure 3 shows profiles of the mean streamwise velocity (normalized by u_m), mean temperature (normalized by T_{ref}), mean

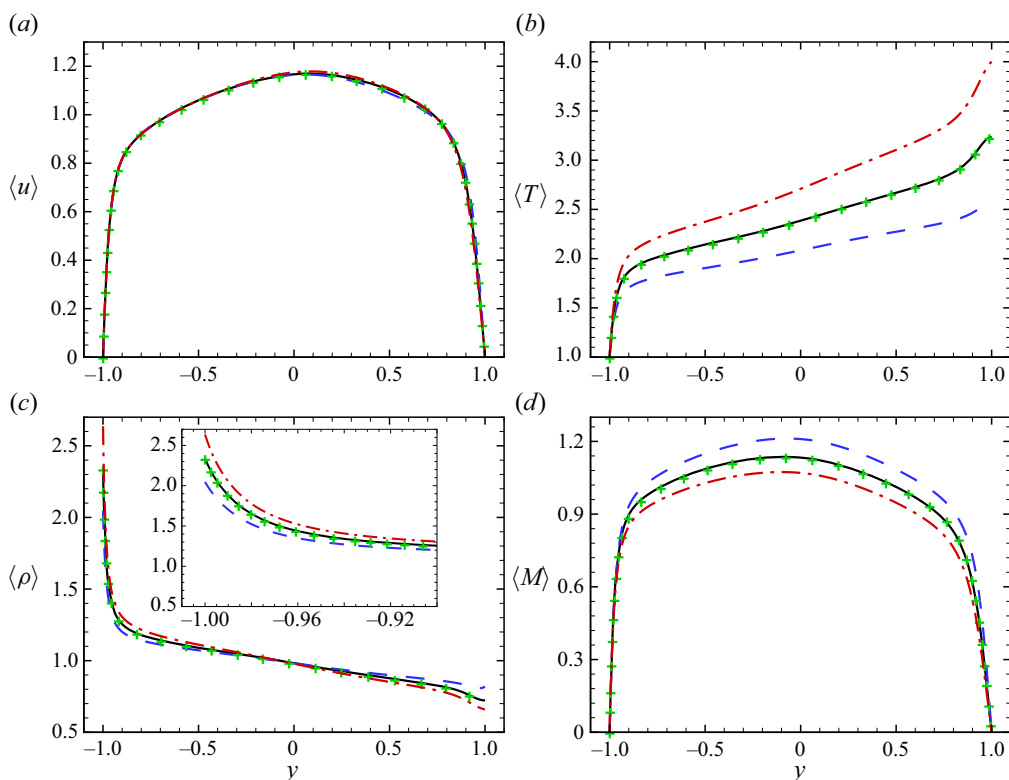


Figure 3. Profiles of (a) the mean streamwise velocity (normalized by u_m), (b) the mean temperature (normalized by T_{ref}), (c) the mean density (normalized by ρ_m) and (d) the local mean Mach number $\langle M \rangle = \langle u \rangle(y) / \langle a \rangle(y)$ from TAd, T25, T32 and T40 in global coordinates, where $\langle a \rangle(y) = \sqrt{\gamma R \langle T \rangle(y)}$ is the local sound speed. The inset in (c) shows a zoomed-in view of the behaviour near the bottom wall.

density (normalized by ρ_m) and local mean Mach number $\langle M \rangle = \langle u \rangle(y) / \langle a \rangle(y)$ from TAd, T25, T32 and T40 in global coordinates. It is seen that all the profiles from the four cases are asymmetric about the central plane, i.e. $y = 0$. Since the thermal boundary conditions at the walls are exerted at the temperature field, the mean temperature profiles from the four cases are clearly asymmetric. The mean temperature first increases rapidly near the bottom wall, and then it increases approximately linearly with y in the core region. Near the top wall, the behaviours of the mean temperature are different, depending on the thermal boundary condition there ($T_{w,t}/T_L$).

The mean density in figure 3(c) behaves in a manner inverse to that of the mean temperature. That is, it decreases rapidly near the bottom wall and then decreases slowly further away from the bottom wall. Compared with the mean temperature and density profiles, the mean streamwise velocity profiles, as well as $\langle M \rangle$, are only slightly asymmetric. When the mean streamwise velocities are normalized by u_m , the mean profiles are very close to each other in the core region at the fixed Re and Ma , whereas the wall frictions at the two walls show some difference, which can be inferred from the Re_τ values listed in table 2. When the wall friction differences are considered, i.e. the mean velocity is rescaled by using u_τ , differences can be observed among TAd (or T32), T25 and T40 in the ‘log-law’ region near both walls, as depicted in figure 4(a,d). It is also seen from these two plots that u^+ values from the four cases deviate from the incompressible profile near the bottom wall, whereas they are very close to the incompressible one near the top wall.

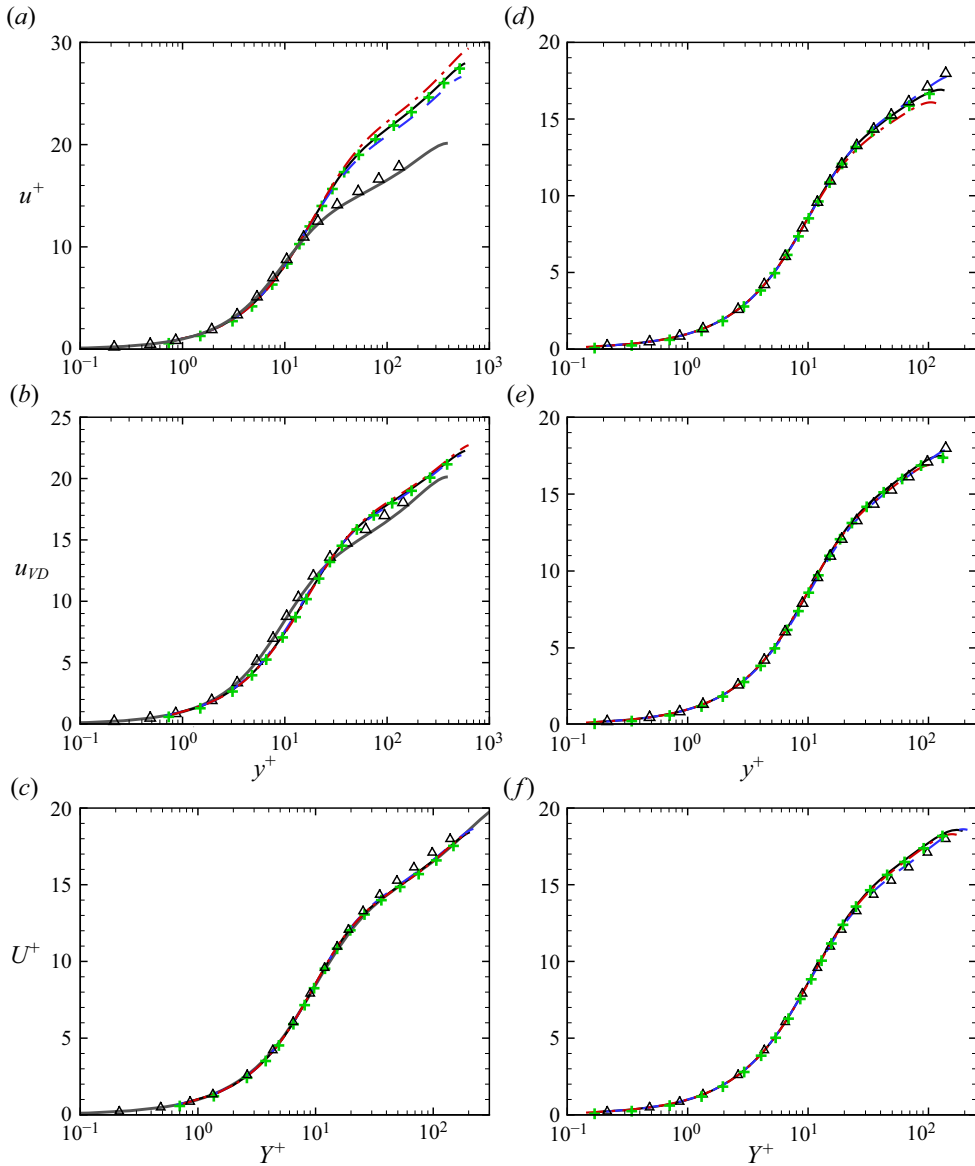


Figure 4. Mean velocity profiles from the four cases for (a–c) the bottom half and (d–f) the top half: (a,d) u^+ versus y^+ ; (b,e) u_{VD} versus y^+ ; (c,f) U^+ versus Y^+ . The incompressible DNS results at $Re_\tau = 180$ (triangles) and 395 (thick grey lines in (a–c)) from Moser, Kim & Mansour (1999) are shown as reference.

In compressible wall-bounded flows, various transformations have been introduced to account for the mean property variations, such as the ‘Van Driest (VD) transformation’ (Van Driest 1951), where the transformed velocity is

$$u_{VD} = \int_0^{u^+} \left(\frac{\bar{\rho}}{\rho_w} \right)^{1/2} du^+, \quad (3.1)$$

and the TL transformation proposed by Trettel & Larsson (2016), where

$$Y^+ = \frac{y}{\delta_v^*}, \tag{3.2}$$

$$U^+ = \int_0^{u^+} \left(\frac{\bar{\rho}}{\rho_w} \right)^{1/2} \left[1 + \frac{1}{2} \frac{1}{\bar{\rho}} \frac{d\bar{\rho}}{dy} y - \frac{1}{\bar{\mu}} \frac{d\bar{\mu}}{dy} y \right] du^+. \tag{3.3}$$

Trettel & Larsson (2016) summarized the status of the VD transformation and reported that it works very well for adiabatic walls up to $Ma = 20$, while its accuracy deteriorates for increasingly non-adiabatic walls. On the other hand, the TL transformation can produce an excellent collapse of the mean velocity profile at different Re , Ma and wall heat transfer rates. Figure 4(b,c) show the VD-transformed velocity u_{VD} versus y^+ and the TL-transformed velocity U^+ versus Y^+ , respectively, near the bottom wall. The corresponding transformed profiles near the top wall are shown in figure 4(e,f). The incompressible mean velocity profiles in turbulent channel flow at $Re_\tau = 180$ and 395 (Moser *et al.* 1999) are also shown for reference. As expected, clear deviations between u_{VD} and u^+ (the incompressible DNS data) can be observed at the non-adiabatic bottom wall side. These deviations include a thickened buffer layer and an upward shift of the log-law intercept (Trettel & Larsson 2016). The TL-transformed velocities U^+ from the four cases collapse excellently and match very well with the incompressible DNS data at $Re_\tau = 395$ in the range $Y^+ \leq 220$. The top wall is either adiabatic or weakly non-adiabatic in all four cases. As a result, the collapse of u_{VD} and U^+ is successful. These transformed mean velocity behaviours are consistent with the recent findings of Huang *et al.* (2023).

The r.m.s. profiles of the three velocity components can also be studied. If they were normalized by u_m and shown in the global coordinate, only small deviations between cases T25, T32 (or TAd) and T40 can be observed, mostly near the top wall (not shown for brevity). In compressible turbulent channel flows with symmetric isothermal walls, Coleman *et al.* (1995) reported that the difference of the r.m.s. velocity fluctuations between the non-zero-Mach-number case and incompressible cases increased with Mach number when normalized by conventional wall variables, whereas the collapse was much better when the semi-local scaling, suggested by Huang *et al.* (1995), was adopted. Following the studies in Coleman *et al.* (1995), the r.m.s. profiles of three velocity components in the inner coordinate, normalized by u_τ at the nearest wall, as well as in the semi-local coordinate, normalized by u_τ^* from the nearest wall, from the two halves of the channel are shown in figure 5. In the inner coordinate, as shown in figure 5(a,b), the profiles from the four cases are quite close to each other in the near-wall region with $y^+ < 10$, and are the same for both halves of the channel. For $y^+ > 10$ in the bottom half, the r.m.s. values of the three velocity components are larger for the case with higher $T_{w,t}$. The trend is opposite for $y^+ > 10$ in the top half, where the r.m.s. values of the three velocity components are smaller for the case with higher $T_{w,t}$. Nevertheless, no obvious difference can be observed for the r.m.s. profiles of the three velocity components between T32 and TAd in both halves, which again shows that the substitution of the adiabatic condition by the pseudo-adiabatic condition will not change the velocity statistics. In the semi-local coordinate, as shown in figure 5(c,d), the deviations between the cases with different $T_{w,t}$ become negligible in both halves, illustrating the superiority of the semi-local scaling over the classical wall units in the present problems. It should be noted that the collapsed profiles still deviate from the incompressible ones at $Re_\tau = 180$ in the bottom half, which is similar to observations in compressible turbulent channels with symmetric isothermal walls (Coleman *et al.* 1995; Modesti & Pirozzoli 2016).

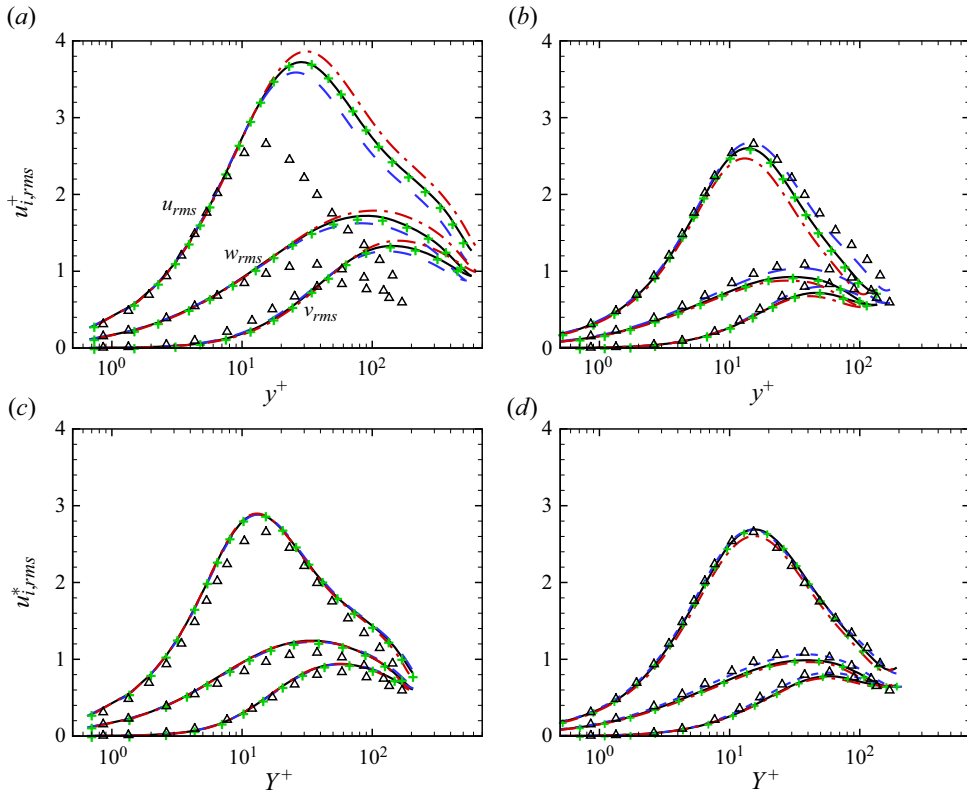


Figure 5. Rescaled r.m.s. values of velocity components from the four cases in (a,b) the classical inner coordinate y^+ (normalized by u_τ at the nearest wall) and (c,d) the semi-local coordinate Y^+ (normalized by u_τ^*) from (a,c) the bottom wall side and (b,d) the top wall side. The incompressible DNS data at $Re_\tau = 180$ from Moser *et al.* (1999) (triangles) are shown for comparison.

The superiority of the semi-local scaling over the classical wall units is also valid for the rescaled Reynolds shear stress and streamwise turbulent heat flux, as shown in figure 6, where the Reynolds shear stress near both walls is normalized by τ_w at the nearest wall, and in figure 7, where the streamwise turbulent heat flux in the bottom wall side is normalized by $\rho_w u_\tau T_\tau = \bar{\rho} u_\tau^* T_\tau^* = q_w / C_p$ at the bottom wall. Since $q_w = 0$ ($q_w \approx 0$) at the adiabatic (quasi-adiabatic) wall, the inner/semi-local rescaled streamwise turbulent heat flux in the top half is not shown. From the figures, it is evident that with the semi-local scaling, the collapse behaviours of the Reynolds shear stress and the streamwise turbulent heat flux are much better. For the streamwise turbulent heat flux, although the rescaled ones do not collapse onto each other, their peak locations are almost the same at $Y^+ \approx 15$.

Now, we turn to the mean temperature profiles again. Following the strategy proposed by Tamano & Morinishi (2006), the mean temperature $\bar{T} - T_L$ is rescaled by the temperature difference between the two walls, $\Delta T = T_{w,t} - T_L$, and the results from our four cases are shown in figure 8(a). The results of the I-PA case at $Ma = 1.5$, $Re = 3000$ and $T_{w,t}/T_L \approx 2.4$ from Tamano & Morinishi (2006) and the I-A case at $Ma = 1.56$ and $Re = 6545$ from Lusher & Coleman (2022a) are also shown for comparison. It is evident that the rescaled mean temperature profiles of the present I-A case and the corresponding I-PA case match well with each other, and they also collapse onto the

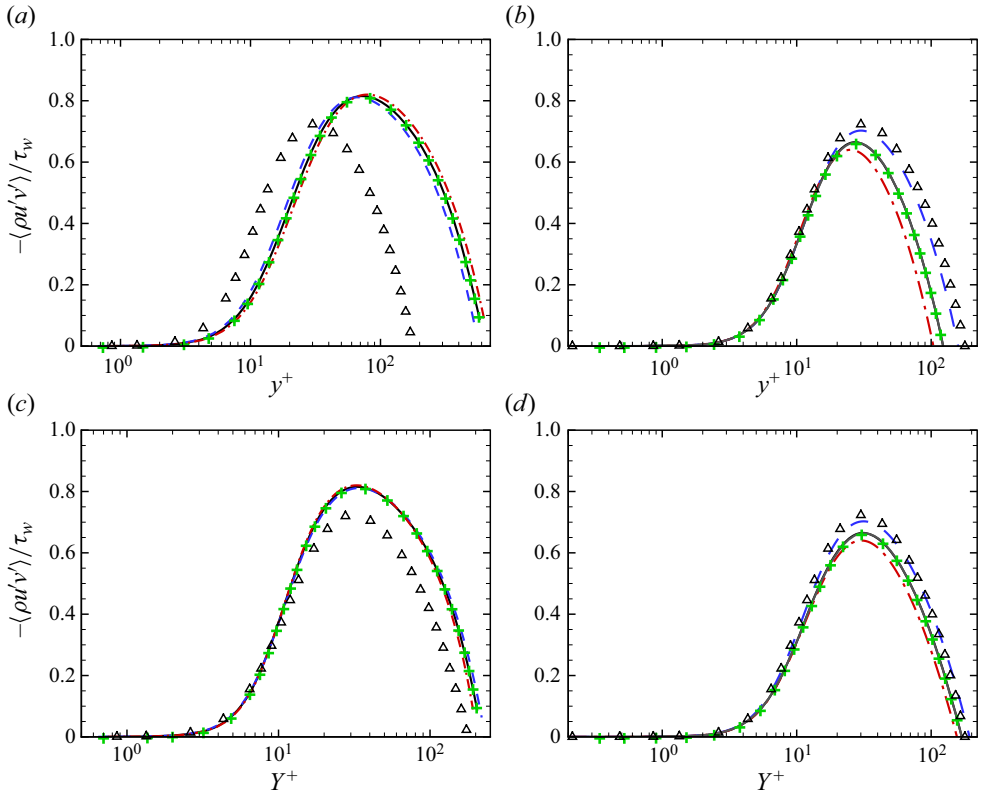


Figure 6. Reynolds shear stress rescaled by τ_w from the four cases in (a,b) the classical inner coordinate y^+ and (c,d) the semi-local coordinate Y^+ from (a,c) the bottom wall side and (b,d) the top wall side. The incompressible DNS data at $Re_\tau = 180$ from Moser *et al.* (1999) (triangles) are shown for comparison.

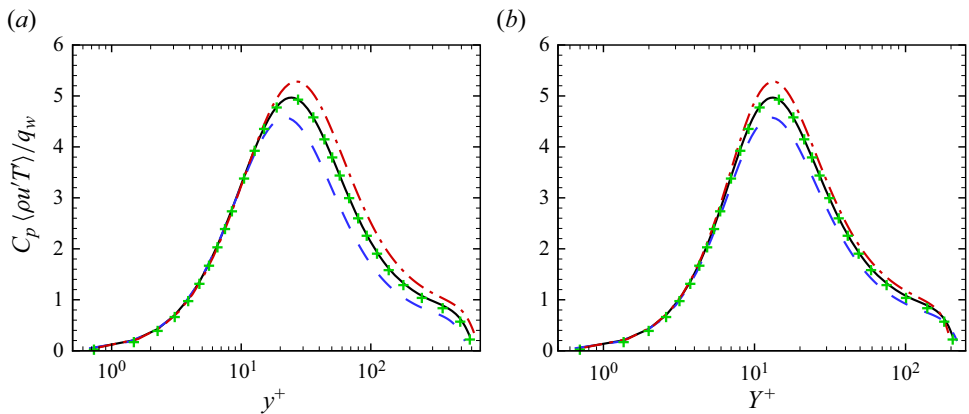


Figure 7. Streamwise turbulent heat flux near the bottom wall side rescaled by $q_w/C_p = \rho_w u_\tau T_\tau = \bar{\rho} u_\tau^* T_\tau^*$ at the bottom wall from the four cases in (a) the classical inner coordinate y^+ and (b) the semi-local coordinate Y^+ .

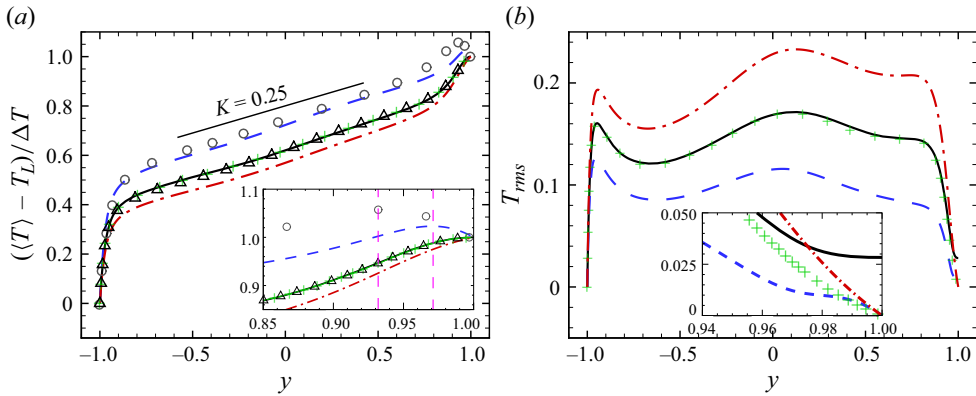


Figure 8. (a) Mean temperature profiles rescaled by $\Delta T = T_{w,t} - T_L$ from the present four cases. The results of the I-PA case at $Ma = 1.5$, $Re = 3000$ and $T_{w,t}/T_L \approx 2.4$ (circles) from Tamano & Morinishi (2006) as well as the I-A case at $Ma = 1.56$ and $Re = 6545$ (triangles) from Lusher & Coleman (2022a) are also shown. The inset shows a zoomed-in plot near the top wall, and the two dashed vertical lines show the locations of the two local peaks. (b) The r.m.s. profiles of temperature fluctuations from the present four cases (normalized by T_{ref}). The inset shows a zoomed-in plot near the top wall.

I-A case from Lusher & Coleman (2022a) at similar Re and Ma , demonstrating that the present simulations are reliable, and that the mean temperature differences between the I-A case and the corresponding I-PA case are negligible. The results presented here differ significantly from those reported in Tamano & Morinishi (2006), where the rescaled mean temperature profiles of their I-A case and the corresponding I-PA case showed a noticeable difference. It is believed that $T_{w,t}/T_L$ was underdetermined in the I-A case in Tamano & Morinishi (2006) due to the simulation not reaching a stationary state, which was understandable given the computational limitations at the time. Lusher & Coleman (2022a) found a significant energy imbalance in Tamano & Morinishi (2006). Figure 8(a) shows that the rescaled mean temperature profiles from the different cases follow a similar trend in the central bulk region, i.e.

$$\frac{\langle T \rangle - T_L}{\Delta T} = Ky + C_T. \quad (3.4)$$

Here, $K \approx 0.25$ is the slope of the rescaled mean temperature profile and C_T is the intercept of the linear temperature profile, which depends on Ma and Re as well as ΔT (or $T_{w,t}$). If we denote by T_A and $C_{T,A}$ the mean temperature at the adiabatic wall in the I-A case and the corresponding intercept, respectively, then $C_T > C_{T,A}$ when $T_{w,t} < T_A$, and vice versa. Near the top wall, the behaviours of the different cases show diverse trends. For the adiabatic and quasi-adiabatic cases, the mean temperature gradient at the top wall is nearly zero. For the cases with $T_{w,t}/T_L < 3.234$, i.e. T25 and the case at $Ma = 1.5$, $Re = 3000$ and $T_{w,t}/T_L \approx 2.4$ from Tamano & Morinishi (2006), the mean temperature gradient at the top wall is negative, that is, the heat will be transferred out from the wall. A local peak of the mean temperature exists near the top wall for these two cases, as was reported in Tamano & Morinishi (2006), and the peak location is closer to the top wall if $T_{w,t}$ is closer to T_A . For the case with $T_{w,t}/T_L > 3.234$, i.e. T40, the mean temperature gradient at the top wall is positive, and the heat will be transferred into the fluid through the wall.

We show in figure 8(b) the r.m.s. profiles of temperature fluctuations from the present four cases. The figure shows clear differences between the three cases, i.e. T25 and

T40, and the higher the $T_{w,t}$, the larger the T_{rms} in the bulk region, whereas the deviations between T32 and TAd are negligible except near the top wall, as shown in the inset in figure 8(b), where it allows fluctuation of temperature at the top wall for TAd but does not for T32. In Tamano & Morinishi (2006), they reported an additional maximum in the region close to the top high-temperature wall, and it was believed to be produced by the maximum of the mean temperature near the high-temperature wall. Nevertheless, there is no extra maximum near the top wall in our results.

Previous studies have shown that in traditional compressible channel flows with symmetric isothermal walls, the mean temperature–velocity relation proposed by Zhang *et al.* (2014) is effective when the edge location is chosen as the channel centre (Modesti & Pirozzoli 2016; Yu *et al.* 2019; Yao & Hussain 2020). However, this temperature–velocity relation is no longer valid in cases with asymmetric thermal walls, unless the edge location is very close to the walls (not shown here). A direct challenge arises from the asymmetric thermal walls.

4. Energy transfers

In this section, we investigate the energy transfer between the Favre-averaged mean-flow kinetic energy $\{K_m\} = \{u_i\}^2/2$, the Favre-averaged turbulent kinetic energy $\{k\} = \{u'_i u'_i\}/2$ and the Favre-averaged mean internal energy $\{e_m\} = C_v\{T\}$ in the four cases. We revise the analyses of Morinishi *et al.* (2004) and Tamano & Morinishi (2006) by using our new data to study the three budget equations of $\{K_m\}$, $\{k\}$ and $\{e_m\}$.

4.1. Budget equations of $\{k\}$, $\{K_m\}$ and $\{e_m\}$

The budget equation of turbulent kinetic energy $\{k\}$ (Huang *et al.* 1995; Morinishi *et al.* 2004) is

$$P_k + D_k - \varepsilon_k + \underbrace{C_{k1} + C_{k2} + C_{k3}}_{C_k} = 0, \tag{4.1}$$

where

$$P_k = -\overline{\rho u'' v''} \partial \tilde{u} / \partial y, \tag{4.2}$$

$$\varepsilon_k = \overline{\tau'_{ij} \partial u'_i / \partial x_j}, \tag{4.3}$$

$$D_k = \partial \left(\overline{\tau'_{i2} u'_i} - \overline{p' v'} - \frac{1}{2} \overline{\rho u'_i u'_i v''} \right) / \partial y, \tag{4.4}$$

$$C_{k1} = -\overline{v''} \partial \bar{p} / \partial y, \quad C_{k2} = \overline{u'_i} \partial \overline{\tau'_{i2}} / \partial y, \quad C_{k3} = \overline{p' \partial u'_j / \partial x_j}. \tag{4.5a-c}$$

Here, P_k is the turbulent production term, ε_k is the dissipation per unit volume, D_k is the diffusion term and C_k is the compressibility term, which is the sum of three terms C_{k1} , C_{k2} and C_{k3} .

The budget equation of mean-flow kinetic energy $\{K_m\}$ (Huang *et al.* 1995; Morinishi *et al.* 2004) is

$$D_{K_m} - P_k - \varepsilon_{K_m} - C_{k1} - C_{k2} + P_{K_m} + f_{K_m} = 0, \tag{4.6}$$

where

$$D_{K_m} = \partial (\overline{\tau'_{i2} \bar{u}_i} - \bar{p} \bar{v} - \overline{\rho u''_i v'' \bar{u}_i}) / \partial y, \tag{4.7}$$

$$\varepsilon_{K_m} = \overline{\tau'_{i2} \partial \bar{u}_i / \partial y}, \tag{4.8}$$

$$P_{K_m} = \bar{p} \partial \bar{v} / \partial y. \tag{4.9}$$

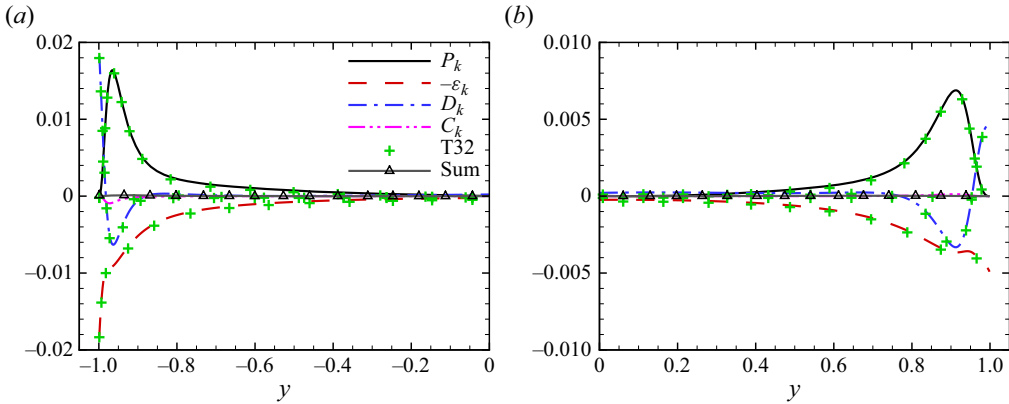


Figure 9. Turbulent kinetic energy budget terms (normalized by $\rho_m u_m^3/h$) in the TAd case near (a) the bottom half and (b) the top half. The corresponding terms from the T32 case are also shown with plus signs.

Here, D_{Km} is the mean-flow diffusion term, ε_{Km} is the mean-flow dissipation per unit volume, P_{Km} is the mean-flow pressure work and f_{Km} is the work of the external force.

The budget equation of the mean internal energy $\{e_m\}$ (Huang *et al.* 1995; Morinishi *et al.* 2004) is

$$D_{em} + \varepsilon_{Km} + \varepsilon_k - P_{Km} - C_{k3} = 0, \tag{4.10}$$

where

$$D_{em} = -\partial(C_v \overline{\rho T'' v''})/\partial y - \partial \overline{q_2}/\partial y \tag{4.11}$$

is the total diffusion term, including the turbulent diffusion and molecular diffusion. It is easily seen from (4.1), (4.6) and (4.10) that there are seven terms which are responsible for the energy transfers among $\{k\}$, $\{K_m\}$ and $\{e_m\}$, and they are P_k , ε_k , C_{k1} , C_{k2} , C_{k3} , ε_{Km} and P_{Km} (Huang *et al.* 1995; Morinishi *et al.* 2004).

4.2. Energy transfer near both walls

We first study the turbulent kinetic energy budget for the TAd case in the bottom and top halves, and the results are shown in figure 9(a,b), respectively, where the budget terms are normalized by $\rho_m u_m^3/h$. The balance, $P_k - \varepsilon_k + D_k + C_k$ (triangles), is almost zero in the whole channel, which confirms that our simulation has reached the fully developed state. From figure 9, it is seen that the dominant terms for $\{k\}$ in the near-wall region are P_k , ε_k and D_k , while the compressibility term C_k is relatively small. The term P_k is positive, ε_k is negative, whereas D_k is positive in the wall's vicinity and then becomes negative as the wall distance increases until it changes sign again further away from the wall. This scenario is the same for both halves of the channel, although the magnitudes of the terms near the top wall are around half of those near the bottom wall. These observations are consistent with those reported in Morinishi *et al.* (2004). As a comparison, we also show in figure 9 the corresponding budget terms from the T32 case, and it is evident that the four terms (P_k , $-\varepsilon_k$, D_k , C_k) match very well with those from the TAd case, again illustrating that the statistics of the turbulent flow field of an I-A case and its corresponding I-PA case are also the same.

Morinishi *et al.* (2004) carefully studied the seven energy exchange/transfer terms and pointed out that the compressibility terms C_{k1} and C_{k3} are negligible close to both the isothermal and the adiabatic walls. In the present study, we have also studied

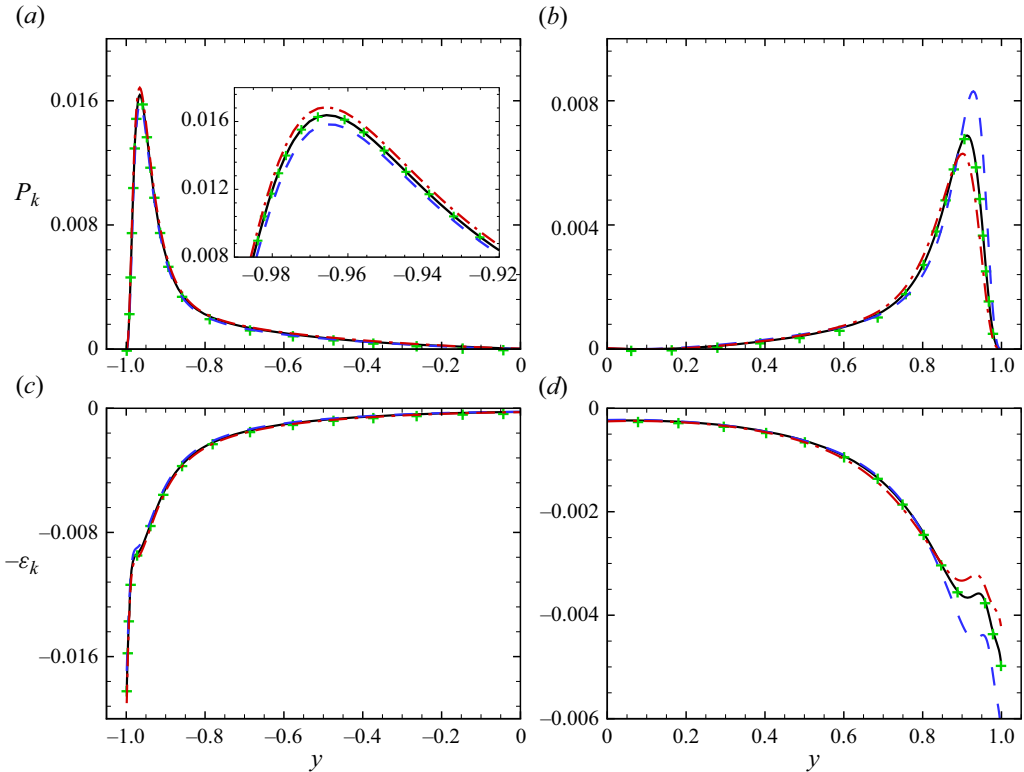


Figure 10. Wall-normal distributions of (a,b) P_k and (c,d) $-\varepsilon_k$ from the four cases. All terms are normalized by $\rho_m u_m^3/h$. (a,c) The bottom half; (b,d) the top half. The inset in (a) shows a zoomed-in plot.

the seven energy exchange/transfer terms in both halves of the channel from the four cases. The wall-normal distributions of P_k and $-\varepsilon_k$, $-\varepsilon_{Km}$ and P_{Km} , and C_{k2} are shown in figures 10–12, respectively. The terms C_{k1} and C_{k3} , which are at least two orders of magnitude smaller than C_{k2} , are not shown. According to figures 10–12, it is evident that P_k is positive while $-\varepsilon_k$ and $-\varepsilon_{Km}$ are negative in the whole channel for all four cases, indicating that their effects on transferring energy are the same near both the low-temperature and the high-temperature (as well as the adiabatic) walls. On the other hand, P_{Km} and C_{k2} are obviously negative near the bottom low-temperature wall, whereas they are positive near the top high-temperature wall, illustrating that they behave differently near the low-temperature and high-temperature walls. Near the bottom low-temperature wall, P_{Km} transfers energy from $\{K_m\}$ to $\{e_m\}$, whereas C_{k2} transfers kinetic energy from $\{k\}$ to $\{K_m\}$. Near the top high-temperature wall, P_{Km} transfers energy from $\{e_m\}$ to $\{K_m\}$, whereas C_{k2} transfers kinetic energy from $\{K_m\}$ to $\{k\}$. These observations are the same as those for the I–A case reported in Morinishi *et al.* (2004). The different values of $T_{w,t}$ on the high-temperature wall not only induce obvious deviations (in magnitude) near the high-temperature side, but also can result in some difference near the bottom low-temperature side. Nevertheless, $T_{w,t}$ (when it is high enough) will not change the basic behaviour of the energy exchange/transfer among $\{K_m\}$, $\{k\}$ and $\{e_m\}$.

From the above analysis, an intuitive energy exchange/transfer diagram can be constructed, and it is shown in figure 13, where figure 9(a,b) represent the bottom low-temperature side and the top high-temperature side, respectively. The energy exchange

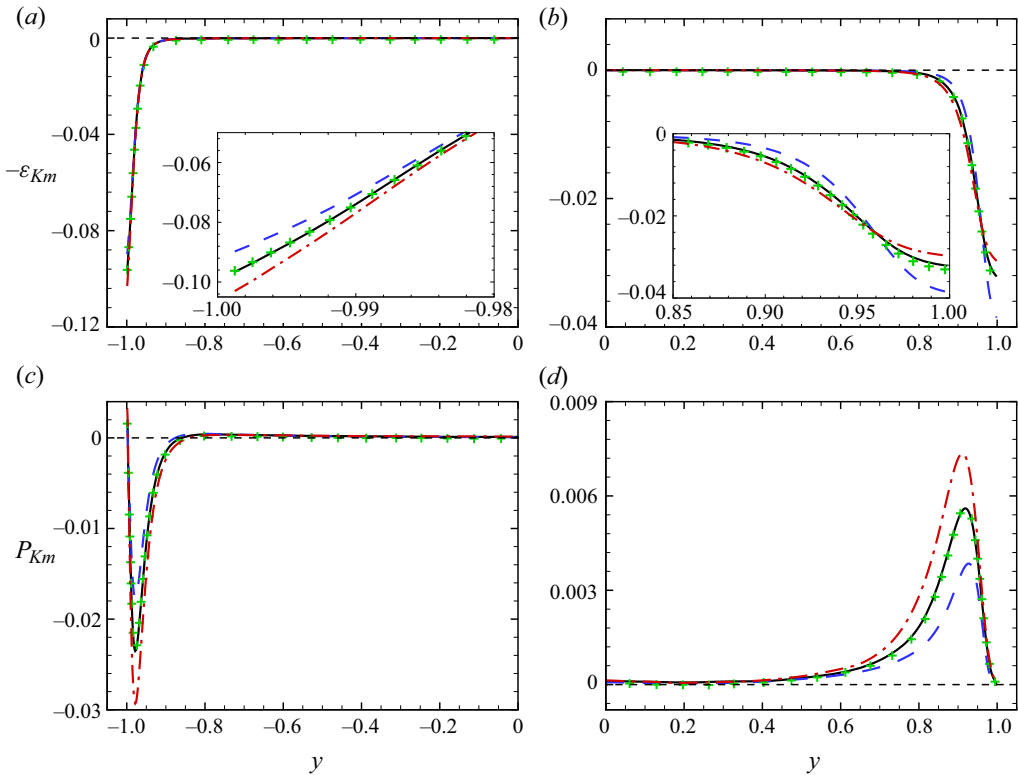


Figure 11. Wall-normal distributions of (a,b) $-\varepsilon_{Km}$ and (c,d) P_{Km} from the four cases. All terms are normalized by $\rho_m u_m^3/h$. (a,c) The bottom half; (b,d) the top half. The insets in (a,b) show zoomed-in plots.

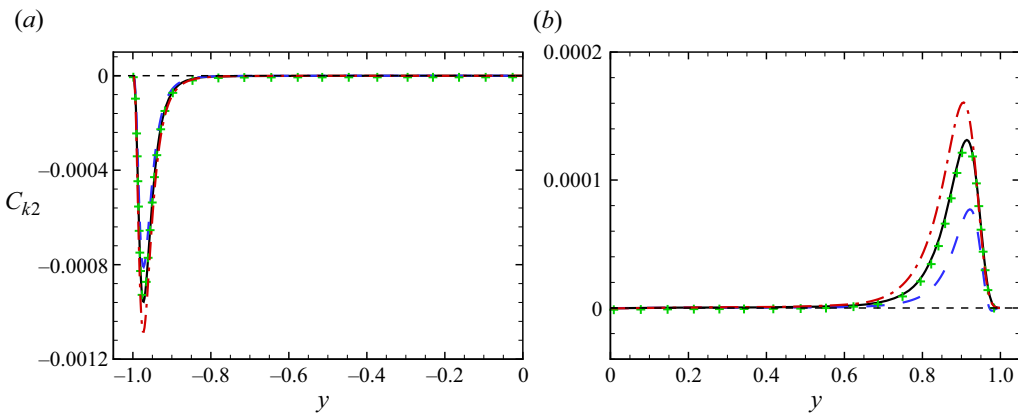


Figure 12. Wall-normal distributions of C_{k2} from the four cases. All terms are normalized by $\rho_m u_m^3/h$. (a) The bottom half; (b) the top half.

terms C_{k1} and C_{k3} are negligible in all four cases when they reach their statistically stationary states. The unidirectional transfer terms P_k , ε_k and ε_{Km} are the same near both walls, whereas the unidirectional transfer terms P_{Km} and C_{k2} have opposite transferring directions near the bottom low-temperature side and the top high-temperature side. Furthermore, the four cases have almost the same results, which indicates that the high

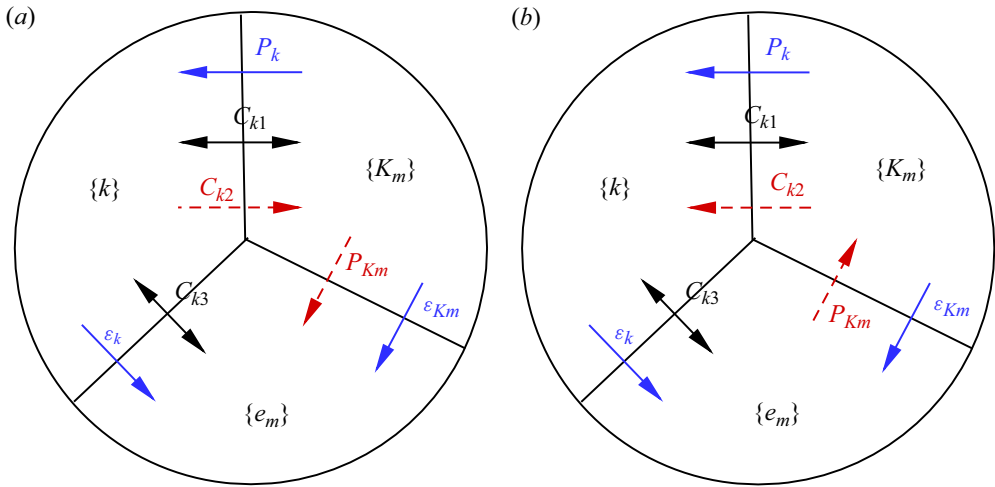


Figure 13. Energy exchange/transfer among $\{k\}$, $\{K_m\}$ and $\{e_m\}$ near (a) the bottom low-temperature side and (b) the top high-temperature side. A term M with $A \leftrightarrow B$ means that it mutually exchanges energy between A and B . A term M with $A \rightarrow B$ means that it transfers energy from A to B , and the directions of the energy transfer are the same near both sides. A term M with $A \dashrightarrow B$ means that it transfers energy from A to B and the directions of the energy transfer are opposite near the two sides.

$T_{w,t}$ at the upper wall, whether it is set by the input or induced by the adiabatic wall boundary, is the crucial reason for the changes in the energy transfer direction of P_{K_m} and C_{k2} .

5. Analysis of wall heat transfer

In compressible channels with periodic boundary conditions in wall-parallel directions, the total energy is conserved, and energy exchange occurs on the wall. Many researchers have studied symmetric isothermal channels where there is no temperature difference between the two walls. However, wall heat transfer behaviours in compressible channels with asymmetric thermal wall conditions have not been studied, and this section is devoted to this problem.

5.1. Heat transfer modes in a compressible channel with asymmetric thermal walls

In a compressible channel with asymmetric thermal walls, the heat transfer property of the high-temperature wall depends largely on its wall temperature $T_{w,t}$, whereas the heat transfer at the low-temperature wall is the same, i.e. transferring heat out of the channel through the wall. This can be easily seen from the mean temperature profiles shown in figures 3(b) and 8. It is evident that there are three kinds of heat transfer modes in such a system. If we denote by T_A the mean temperature at the adiabatic wall in an I–A case at prescribed Re and Ma , the three modes can be categorized as the sub-adiabatic, quasi-adiabatic and super-adiabatic modes, respectively, as depicted in figure 14(a–c). For $T_L \leq T_{w,t} < T_A$, i.e. the sub-adiabatic mode shown in figure 14(a), there is a peak of the mean temperature profile, T_{max} , which is located between the channel centre and the top wall while satisfying $dT/dy = 0$, and heat is transferred out of the fluid system through both walls. A special case is the channel with symmetric isothermal walls, i.e. $T_{w,t} = T_L$. In such a situation, T_{max} is located at the channel centre according to the symmetry, and an

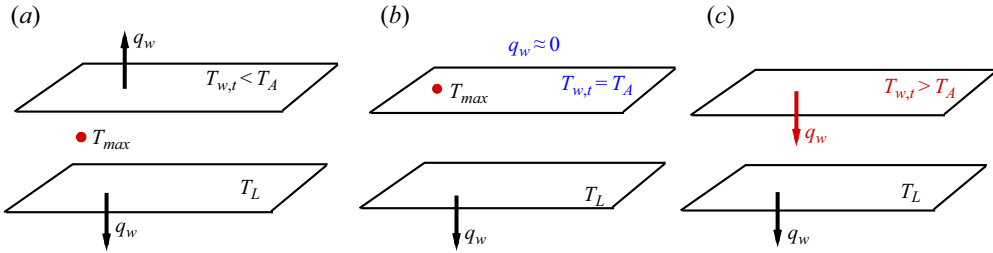


Figure 14. Heat transfer modes between the fluid and the walls in a compressible channel with asymmetric thermal walls. (a) Sub-adiabatic state $T_L \leq T_{w,t} < T_A$ (T_A is the mean temperature at the adiabatic wall in the I–A case), where heat is transferred out of the fluid system through both walls. (b) Adiabatic (quasi-adiabatic) state $T_{w,t} = T_A$, where heat is transferred out of the fluid system through the bottom wall and almost no net heat exchange occurs between the top wall and the fluid. (c) Super-adiabatic state $T_{w,t} > T_A$, where heat is transferred into the fluid system through the top wall and is transferred out of the fluid system through the bottom wall.

empirical scaling of T_{max} was proposed by Song *et al.* (2022) recently. When $T_{w,t} = T_A$, i.e. the quasi-adiabatic mode shown in figure 14(b), T_{max} is located at the top wall where $q_w \approx 0$ or $dT/dy \approx 0$, and no net heat exchange occurs between the top wall and the fluid. Heat can only be transferred out of the fluid system through the bottom wall. When $T_{w,t} > T_A$, i.e. the super-adiabatic mode shown in figure 14(c), T_{max} is again located at the top wall. However, $dT/dy \neq 0$ and heat is transferred to the fluid from the top wall, and it can only be transferred out of the fluid system through the bottom wall. Therefore, T_A can be viewed as an important quantity for separating the different heat transfer modes.

5.2. Wall heat flux analysis

Now we investigate the wall heat flux by using integral analysis (Zhang & Xia 2020; Sun *et al.* 2021; Zhang, Song & Xia 2021; Wenzel, Gibis & Kloker 2022; Xu, Wang & Chen 2022). In the present study, we start with the internal energy equation (Mittal & Girimaji 2019), and its Reynolds-averaged form can be expressed as (see also (4.10))

$$\frac{\partial}{\partial y} (\bar{q}_y + C_v \overline{\rho T'' v''}) = \underbrace{-\bar{p} \frac{\partial \bar{v}}{\partial y} - \overline{p' \frac{\partial u'_k}{\partial x_k}}}_{\bar{P}_d} + \underbrace{\bar{\tau}_{i2} \frac{\partial \bar{u}_i}{\partial y} + \overline{\tau'_{ij} \frac{\partial u'_i}{\partial x_j}}}_{\bar{V}_a}. \quad (5.1)$$

Here, $\bar{P}_d = -P_{Km} - C_{k3}$ and $\bar{V}_a = \varepsilon_{Km} + \varepsilon_k$, where the four terms are the energy transfer/exchange terms between $\{k\}$ and $\{e_m\}$ and between $\{K_m\}$ and $\{e_m\}$ in § 4. Integrating (5.1) from -1 to y , we obtain the heat flux balance at an arbitrary wall-normal location y :

$$q_w|_{y=-1} = \bar{q}_y(y) + C_v \overline{\rho T'' v''}(y) - \int_{-1}^y \bar{P}_d(y_1) dy_1 - \int_{-1}^y \bar{V}_a(y_1) dy_1. \quad (5.2)$$

This equation means that the heat transferred into the fluid system through the bottom wall can be estimated through the first law of thermodynamics within the control volume $[-1, y]$, i.e. the heat transferred out of the control volume through the top boundary at location y through the turbulent heat flux $C_v \overline{\rho T'' v''}$ and the mean molecular heat flux \bar{q}_y subtracts the energy generated inside the control volume through the pressure dilatation work and the viscous stress work. Note that if the value of $q_w|_{y=-1}$ is negative, the heat is actually transferred out of the fluid system.

Case	$B_{q,d}$	$B_{q,int}$	Error	$B_{q,P}$	$B_{q,V}$
TAd	-7.065×10^{-2}	-7.007×10^{-2}	0.81 %	-5.609×10^{-5}	-7.002×10^{-2}
T32	-7.003×10^{-2}	-7.005×10^{-2}	-0.03 %	-5.852×10^{-5}	-6.999×10^{-2}
T25	-7.536×10^{-2}	-7.502×10^{-2}	0.45 %	-6.458×10^{-5}	-7.495×10^{-2}
T40	-6.705×10^{-2}	-6.701×10^{-2}	0.06 %	-5.097×10^{-5}	-6.696×10^{-2}

Table 3. Dimensionless wall heat transfer rate B_q . Here, $B_{q,d}$ and $B_{q,int}$ are the calculations where q_{in} is obtained using $q_{in} = q_w|_{y=-1} - q_w|_{y=1}$ and using the integrals on the right-hand side of (5.4), respectively. The error is defined as $(B_{q,d} - B_{q,int})/B_{q,d} \times 100\%$.

Alternatively, we may also integrate (5.1) from y to 1 to obtain

$$q_w|_{y=1} = \bar{q}_y(y) + C_v \overline{\rho T'' v''}(y) + \int_y^1 \overline{P_d}(y_1) dy_1 + \int_y^1 \overline{V_a}(y_1) dy_1, \quad (5.3)$$

which can be physically explained similarly. Considering the special case in (5.2) with $y = 1$, or subtracting (5.3) from (5.2), the total wall heat flux transferred into the fluid system can be obtained:

$$q_{in} = q_w|_{y=-1} - q_w|_{y=1} = - \int_{-1}^1 \overline{P_d} dy - \int_{-1}^1 \overline{V_a} dy, \quad (5.4)$$

or equivalently

$$q_{out} = -q_{in} = q_w|_{y=1} - q_w|_{y=-1} = \int_{-1}^1 \overline{P_d} dy + \int_{-1}^1 \overline{V_a} dy. \quad (5.5)$$

Equation (5.5) indicates that the total heat transfer out of the fluid system through the walls equals the sum of the total pressure dilatation work (the first term on the right-hand side of (5.5)) and the total viscous stress work (the second term on the right-hand side of (5.5)) across the channel. A similar formula was obtained in symmetric compressible turbulent channel flow (Ghosh, Foysi & Friedrich 2010; Zhang *et al.* 2021). If we normalize q_{in} by $C_p \rho_w u_\tau T_{ref}$ at the bottom wall, the dimensionless wall heat transfer rate B_q can be defined, i.e.

$$B_q = \frac{q_{in}}{C_p \rho_w u_\tau T_{ref}} = \frac{q_{in}}{C_p \rho_w u_\tau T_L}. \quad (5.6)$$

Correspondingly, the total pressure dilatation work and total viscous stress work contributions of B_q can be defined as $B_{q,P}$ and $B_{q,V}$, respectively, according to (5.4). In table 3, we have calculated B_q from the four cases based on the temperature gradients on the two walls, i.e. using $q_{in} = q_w|_{y=-1} - q_w|_{y=1}$, as well as that based on the integral analysis, i.e. using the right-hand side of (5.4), and the results strongly suggest that the two estimations match very well with each other, and the relative errors are within 1 %. For the two contribution terms of B_q in the integral analysis, i.e. $B_{q,P}$ and $B_{q,V}$, it is evident from table 3 that the main contribution is $B_{q,V}$, for which the contribution exceeds 99.9 % of the total B_q , and the contribution of $B_{q,P}$ is minor, it being around three orders of magnitude smaller than that of $B_{q,V}$. This conclusion is consistent with results reported for compressible channels of symmetric isothermal walls by Zhang *et al.* (2021) and physical intuition.

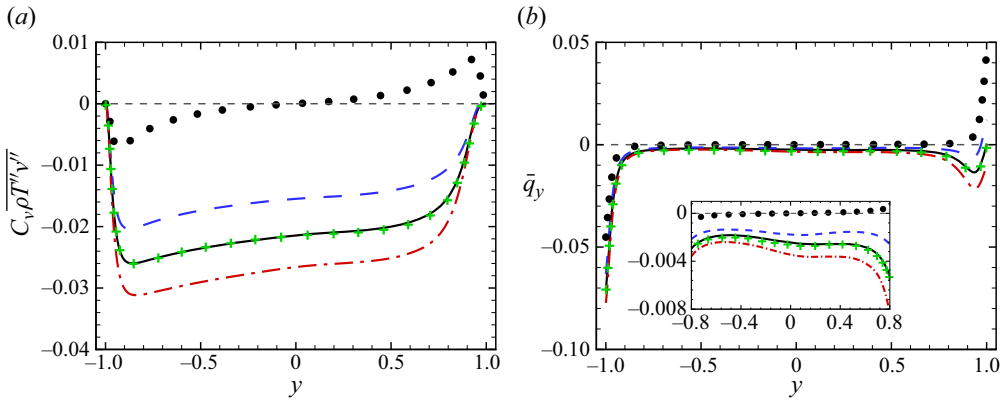


Figure 15. Wall-normal distributions of (a) $C_v \overline{\rho T'' v''}$ and (b) \bar{q}_y from the four cases. The quantities are normalized with $C_p \rho_w T_L u_\tau$ at the bottom wall. The results from a compressible channel with symmetric isothermal walls at $Ma = 1.5$ and $Re = 6000$ (circles) from Zhang & Xia (2020) are also shown for comparison. The inset in (b) shows a zoomed-in plot for $-0.8 \leq y \leq 0.8$.

As discussed above, it can be seen from (5.2), (5.3) and (5.4) that \bar{q}_y and $C_v \overline{\rho T'' v''}$ represent the mean heat transfer across the plane y from the bottom part to the top part of the channel separated by y . If the value is negative, the actual heat transfer direction is from the top part to the bottom part. Figure 15 shows the wall-normal distributions of \bar{q}_y and $C_v \overline{\rho T'' v''}$ from the present four cases. The results from a compressible channel with symmetric isothermal walls at $Ma = 1.5$ and $Re = 6000$ from Zhang & Xia (2020) are also shown for comparison. For the symmetric isothermal case, it is seen that both terms are zero at the channel centre, $y = 0$, indicating that there is no mean heat exchange between the top half and the bottom half of the channel, and that the wall heat flux across the wall can be attributed to the work done by the viscous stress and the pressure dilatation. Furthermore, \bar{q}_y and $C_v \overline{\rho T'' v''}$ are antisymmetric about the channel centre $y = 0$. In the core region with $-0.4 \leq y \leq 0.4$, the heat generated in this region is transferred out mainly through the turbulent heat flux term $C_v \overline{\rho T'' v''}$, whereas the mean molecular heat flux term \bar{q}_y is approximately zero. In contrast, in the near-wall region with $|y| \geq 0.9$, \bar{q}_y becomes important and dominates. For the four cases with asymmetric isothermal walls, \bar{q}_y and $C_v \overline{\rho T'' v''}$ behave very differently, and they are no longer antisymmetric about the channel centre $y = 0$. For $C_v \overline{\rho T'' v''}$, it is negative almost across the channel for all four cases, demonstrating that heat is transferred from the top part down to the bottom part through the plane y , except that a small region with very small positive values exists very close to the top wall for the T25 case (not shown). For \bar{q}_y , similar results are obtained. Among the four cases, the smaller $T_{w,t}$ is, the larger are the absolute values of \bar{q}_y and $C_v \overline{\rho T'' v''}$, that is, more heat is transferred from the top part down to the bottom part through the plane y . Generally, $C_v \overline{\rho T'' v''}$ dominates over \bar{q}_y except very close to the walls. Nevertheless, B_q is smaller since it is defined as the total heat transferred out of the system, which is different from the global-mean heat flux ($\langle q_w^\pm \rangle = (|\langle q_y \rangle|_{y=-1} + |\langle q_y \rangle|_{y=1})/2$) defined by Lusher & Coleman (2022a), and there is heat transferred into the system through the top wall if $T_{w,t} > T_A$, as discussed in § 5.1.

From the above analysis, a physical picture emerges: due to the asymmetry of the thermal wall boundary conditions, the symmetry of the heat transfer property breaks. The heat generated by the work done by the pressure dilatation and viscous stress in the top half

of the channel will be transferred both upward and downward, separated by the location h_0 where \bar{T} reaches its local peak and depends on $T_{w,t}$ (see discussions in § 5.1), through \bar{q}_y and $C_v \rho \overline{T''v''}$. In the bulk region, $C_v \rho \overline{T''v''}$ plays the dominant role, whereas in the near-wall region \bar{q}_y dominates.

5.3. Mathematical relationship between wall heat flux and wall friction

In this section, we derive the relationship between the wall heat flux and the wall friction by using the mean streamwise momentum equation and the mean total energy equation, which are

$$\frac{\partial \overline{\rho u v}}{\partial y} = \frac{\partial \overline{\tau_{12}}}{\partial y} + \bar{f} \tag{5.7}$$

and

$$\frac{\partial \overline{E v}}{\partial y} = -\frac{\partial \overline{p v}}{\partial y} + \frac{\partial \overline{\tau_{i2} u_i}}{\partial y} - \frac{\partial \bar{q}_y}{\partial y} + \overline{u f}, \tag{5.8}$$

respectively.

Equations (5.8) and (5.7) are fully integrated from -1 to 1 . By using the constraints $\int_{-1}^1 \bar{\rho} dy = 2\rho_m$ and $\int_{-1}^1 \overline{\rho u} dy = 2\rho_m u_m$ ($\rho_m = 1, u_m = 1$), we can derive the following equation:

$$q_{in} = q_w|_{y=-1} - q_w|_{y=1} = -(\tau_w|_{y=-1} - \tau_w|_{y=1}) \frac{\int_{-1}^1 \bar{u} dy}{2}. \tag{5.9}$$

Equation (5.9) still works for compressible channels with symmetric isothermal walls, and it can also be derived through the overall energy balance, i.e. the heat transferred into the walls equals the total work done by the driving force (Huang *et al.* 1995). With the definition of the skin-friction coefficient $C_f = 2(\tau_w|_{y=-1} - \tau_w|_{y=1})/(\rho_m u_m^2)$ and $U_{avg} = \int_{-1}^1 \bar{u} dy/2$, we can define the ratio $R_{H,F}$, which is similar to the Reynolds analogy factor, as

$$R_{H,F} = -\frac{B_q}{C_f} = \frac{\gamma - 1}{2} Ma^2 \frac{\rho_m U_{avg}}{\rho_w u_\tau} = \frac{\gamma - 1}{2} Ma^2 \frac{Re}{Re_\tau} \frac{U_{avg}}{u_m}, \tag{5.10}$$

where Re_τ is the friction Reynolds number at the bottom wall, as listed in table 2. Similarly, if the flow is driven by the external force ρf in the streamwise direction, $R_{H,F}$ is slightly modified to

$$R_{H,F} = -\frac{B_q}{C_f} = \frac{\gamma - 1}{2} Ma^2 \frac{\rho_m u_m}{\rho_w u_\tau} = \frac{\gamma - 1}{2} Ma^2 \frac{Re}{Re_\tau}. \tag{5.11}$$

A similar relationship was obtained by Li *et al.* (2019a) for compressible channels with symmetric isothermal walls. Table 4 presents the directly calculated values of C_f , B_q , U_{avg} and $R_{H,F}$ from the present four cases driven by a uniform external force. Here, $R_{H,F}$ is estimated using either B_q and C_f or (5.10). The balance for (5.10) is highly accurate, with relative errors of less than 0.8%, verifying the energy balance in the current simulations. Equation (5.10) also shows that $R_{H,F}$ is dependent on Ma , Re , Re_τ (at the bottom wall) and the ratio U_{avg}/u_m , making it a response parameter. For fixed Ma and Re , changing the value of $T_{w,t}$ will alter the values of Re_τ at the bottom wall and U_{avg}/u_m . From the data listed in tables 2 and 4, it can be seen that U_{avg}/u_m changes slightly with varying $T_{w,t}$, whereas Re_τ at the bottom wall changes greatly. An increase in $T_{w,t}$ can lead to an

Case	$C_{f,d}$	$B_{q,d}$	$-(B_q/C_f)_d$	U_{avg}/u_m	$R_{H,F}$	Error
TAd	1.505×10^{-2}	-7.065×10^{-2}	4.694	1.009	4.657	0.79 %
T32	1.508×10^{-2}	-7.002×10^{-2}	4.643	1.009	4.665	-0.47 %
T25	1.482×10^{-2}	-7.536×10^{-2}	5.085	1.009	5.073	0.24 %
T40	1.548×10^{-2}	-6.705×10^{-2}	4.331	1.010	4.322	0.21 %

Table 4. Numerical results for the skin-friction coefficient C_f and wall heat flux coefficient B_q . The error is defined as $(-(B_q/C_f)_d - R_{H,F})/|(B_q/C_f)_d| \times 100\%$ and $R_{H,F}$ is defined in (5.10).

increase in C_f (and Re_τ at the bottom wall) and a decrease in B_q , and therefore a decrease in $R_{H,F}$.

6. Conclusions

This paper presents DNS results for compressible turbulent channel flows with asymmetric thermal walls at fixed $Re = 6000$ and $Ma = 1.5$. The bottom wall is isothermal and fixed at $T_L = T_{ref}$, while the top wall is either adiabatic (TAd) or isothermal with $T_{w,t}/T_{ref} = 2.5$ (T25), 3.234 (T32, the pseudo-adiabatic case) and 4.0 (T40). The study focuses on examining the similarities and differences between the I–A case and its corresponding I–PA case, as well as the effect of the wall temperature difference between the two isothermal walls. It investigates basic turbulent statistics, the heat transfer between the Favre-averaged mean-flow kinetic energy, the Favre-averaged turbulent kinetic energy and the Favre-averaged mean internal energy, as well as wall heat transfer properties. The findings lead to the following conclusions.

- (1) Almost all turbulent statistics of the cases TAd and T32 are the same, except for the temperature-fluctuation-related quantities, such as T_{rms} , where some differences can be observed in a small region very close to the top wall. This indicates that the I–A case and its corresponding I–PA case are generally equivalent, and thus the isothermal wall boundary with $T_{w,t} = T_A$ can be used to replace the actual adiabatic boundary condition.
- (2) The asymmetry of the thermal walls leads to asymmetry of the flow fields and thermal fields. The profiles of mean velocity, r.m.s. of velocity fluctuations and Reynolds shear stress can be well matched in the lower half of the channel in the local semi-local coordinate, but they are less well matched in the upper half of the channel.
- (3) In terms of energy transfer behaviour, compared with the energy transfer direction near the bottom wall, the mean-flow pressure work term P_{Km} and the compressibility term C_{k2} change their transfer direction near the top wall, regardless of whether it is an adiabatic wall or an isothermal wall with high $T_{w,t}$, indicating that the high $T_{w,t}$ at the upper wall is the crucial factor leading to the changes in the energy transfer direction of P_{Km} and C_{k2} .
- (4) By analysing the direction of heat flux on the top high-temperature wall, it is found that T_A can be used as a criterion to determine the direction of heat flux on the high-temperature sidewall. The turbulent heat flux $C_v \rho \overline{T''v''}$ and the mean molecular heat flux \bar{q}_y are responsible for the heat transfer generated by the pressure dilatation work and the viscous stress work, where the former dominates in the bulk region and the latter is more important in the near-wall region. The findings have the potential

Case	Re_τ	Δx^+	Δy_{min}^+	Δy_{max}^+	Δz^+	Re_τ	Δx^+	Δy_{min}^+	Δy_{max}^+	Δz^+	T_A
Grid-A	585	12.76	0.73	10.15	7.65	135	2.94	0.17	2.34	1.76	3.234
Grid-B	588	12.83	0.43	6.10	5.14	135	2.94	0.10	1.40	1.18	3.242
Grid-C	586	8.52	0.43	6.08	5.12	134	1.95	0.10	1.40	1.18	3.247

Table 5. Baseline grid resolution (Grid-A: $864 \times 240 \times 320$) and refined grid resolutions (Grid-B: $864 \times 400 \times 480$; Grid-C: $1296 \times 400 \times 480$) for the TAd case. The data in columns 2–6 and columns 7–12 are the results normalized by the quantities at the bottom wall ($y = -1$) and top wall ($y = 1$), respectively.

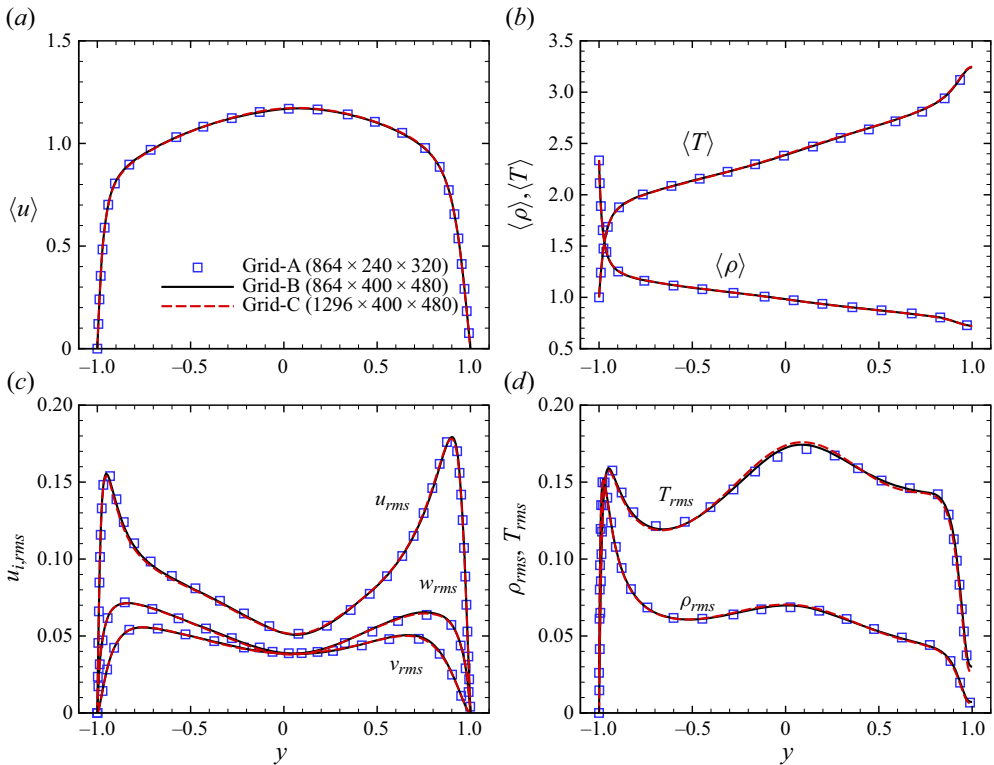


Figure 16. Comparisons between three different grids: (a) mean streamwise velocity (normalized by u_m), (b) mean temperature and density (normalized by T_{ref} and ρ_m , respectively), (c) r.m.s. of the three velocity fluctuations (normalized by u_m) and (d) r.m.s. of temperature and density fluctuations (normalized by T_{ref} and ρ_m , respectively).

to offer new insights and enhance our understanding of heat transfer phenomena related to wall turbulence prediction and control.

In the future, we will investigate the effects of Ma and Re , as well as Pr , on compressible turbulent channel flows with asymmetric thermal walls. Furthermore, we will try to provide a clear explanation for the linear mean temperature profile in the central bulk region and improve the mean temperature–velocity relation. Additionally, this flow problem has the potential to serve as a complementary canonical test case for assessing the various subgrid-scale models and the Reynolds-averaged Navier–Stokes models.

Acknowledgements. The simulations were carried out on the Hygon C86 7185 GPU processors housed at the Kunshan Computing Center.

Funding. The authors gratefully acknowledge support from the National Natural Science Foundation of China (NSFC grant nos. 92152101 and 92152301).

Declaration of interests. The authors report no conflict of interest.

Author ORCID.

 Zhenhua Xia <https://orcid.org/0000-0002-5672-5890>.

Appendix. Grid refinement for the TAd case

To demonstrate the adequacy of the grid used in this study, two additional cases were carried out for the TAd case. Grid refinement was performed in the spanwise and wall-normal directions, as well as in the streamwise direction. The detailed grid resolutions in wall units, based on the values at the nearest wall, are presented in [table 5](#). Here, Grid-A ($864 \times 240 \times 320$) represents the baseline grid, Grid-B ($864 \times 400 \times 480$) is the spanwise and wall-normal refined grid and Grid-C ($1296 \times 400 \times 480$) is the streamwise, spanwise and wall-normal refined grid. [Figure 16](#) displays a comparison of the mean velocity, mean temperature, mean density and r.m.s. of velocity, temperature and density between the baseline grid (Grid-A) and the refined grids (Grid-B and Grid-C). The statistics demonstrate consistency throughout the entire channel for all three grids. It has been found that the variations of $u_\tau^*(y) = \sqrt{|\tau_w|/\bar{\rho}(y)}$ (which are not shown here) along y are quite small under the three grid resolutions. Here, τ_w is based on the value at the nearest wall. This illustrates that the three grids have a minimal effect on u_τ and the inner-scaled flow statistics. Additionally, a direct comparison between our TAd case on Grid-A and the aiB case with $Re = 6545$, $Ma = 1.56$ and $\Delta z^+ = 6.3$ from Lusher & Coleman (2022a) shows excellent agreement. All the previous discussions have demonstrated that our baseline Grid-A is sufficiently accurate to provide reliable data for the current problem.

REFERENCES

- AVELLANEDA, J.M., BATAILLE, F. & TOUTANT, A. 2019 DNS of turbulent low Mach channel flow under asymmetric high temperature gradient: effect of thermal boundary condition on turbulence statistics. *Intl J. Heat Fluid Flow* **77**, 40–47.
- AVELLANEDA, J.M., BATAILLE, F., TOUTANT, A. & FLAMANT, G. 2021 DNS of entropy generation rates for turbulent flows subjected to high temperature gradients. *Intl J. Heat Mass Transfer* **176**, 121463.
- BARANWAL, A., DONZIS, D.A. & BOWERSOX, R.D.W. 2022 Asymptotic behaviour at the wall in compressible turbulent channels. *J. Fluid Mech.* **933**, A28.
- BARANWAL, A., DONZIS, D.A. & BOWERSOX, R.D.W. 2023 Turbulent heat flux in supersonic flows for different thermal boundary conditions. In *AIAA SciTech 2023 Forum*, paper no. 2023-0868. American Institute of Aeronautics and Astronautics.
- BRADSHAW, P. 1977 Compressible turbulent shear layers. *Annu. Rev. Fluid Mech.* **9** (1), 33–52.
- CHEN, X.P. & FEI, F. 2018 Effects of dimensional wall temperature on Reynolds stress budgets in a supersonic turbulent channel flow with thermally perfect gas. *Intl J. Comput. Fluid Dyn.* **32**, 315–325.
- CHENG, C. & FU, L. 2023 Linear-model-based study of the coupling between velocity and temperature fields in compressible turbulent channel flows. *J. Fluid Mech.* **964**, A15.
- CHENG, C., SHYY, W. & FU, L. 2023 Momentum and heat flux events in compressible turbulent channel flows. *Phys. Rev. Fluids* **8**, 094602.
- COLEMAN, G.N., KIM, J. & MOSER, R.D. 1995 Numerical study of turbulent supersonic isothermal-wall channel flow. *J. Fluid Mech.* **305** (305), 159–183.
- FOYSI, H., SARKAR, S. & FRIEDRICH, R. 2004 Compressibility effects and turbulence scalings in supersonic channel flow. *J. Fluid Mech.* **509**, 207–216.
- GATSKI, T. & BONNET, J. 2013 *Compressibility, Turbulence and High Speed Flow*. Academic Press.

- GEROLYMOS, G.A. & VALLET, I. 2023 Scaling of pressure fluctuations in compressible turbulent plane channel flow. *J. Fluid Mech.* **958**, A19.
- GEROLYMOS, G.A. & VALLET, I. 2024 Total and static temperature statistics in compressible turbulent plane channel flow. *J. Fluid Mech.* **978**, A25.
- GHOSH, S., FOYSI, H. & FRIEDRICH, R. 2010 Compressible turbulent channel and pipe flow: similarities and differences. *J. Fluid Mech.* **648**, 155–181.
- GRIFFIN, K.P., FU, L. & MOIN, P. 2021 Velocity transformation for compressible wall-bounded turbulent flows with and without heat transfer. *Proc. Natl Acad. Sci. USA* **118** (34), e2111144118.
- HASAN, A.M., LARSSON, J., PIROZZOLI, S. & PECNIK, R. 2023 Incorporating intrinsic compressibility effects in velocity transformations for wall-bounded turbulent flows. *Phys. Rev. Fluids* **8**, L112601.
- HUANG, P.G., COLEMAN, G.N. & BRADSHAW, P. 1995 Compressible turbulent channel flows: DNS results and modelling. *J. Fluid Mech.* **305**, 185–218.
- HUANG, P.G., COLEMAN, G.N., SPALART, P.R. & YANG, X.I.A. 2023 Velocity and temperature scalings leading to compressible laws of the wall. *J. Fluid Mech.* **977**, A49.
- LESSANI, B. & PAPALEXANDRIS, M.V. 2008 Numerical study of turbulent channel flow with strong temperature gradients. *Intl J. Numer. Meth. Heat Fluid Flow* **18** (3–4), 545–556.
- LI, W.P., FAN, Y.T., MODESTI, D. & CHENG, C. 2019a Decomposition of the mean skin-friction drag in compressible turbulent channel flows. *J. Fluid Mech.* **875**, 101–123.
- LI, X., TONG, F.-L., YU, C.-P. & LI, X.-L. 2019b Statistical analysis of temperature distribution on vortex surfaces in hypersonic turbulent boundary layer. *Phys. Fluids* **31** (10), 106101.
- LIANG, X. & LI, X.L. 2015 Direct numerical simulation on Mach number and wall temperature effects in the turbulent flows of flat-plate boundary layer. *Commun. Comput. Phys.* **17** (1), 189–212.
- LUSHER, D.J. & COLEMAN, G.N. 2022a Numerical study of compressible wall-bounded turbulence – the effect of thermal wall conditions on the turbulent Prandtl number in the low-supersonic regime. *Intl J. Comput. Fluid Dyn.* **36** (9), 797–815.
- LUSHER, D.J. & COLEMAN, G.N. 2022b Numerical study of the turbulent Prandtl number in supersonic plane-channel flow – the effect of thermal boundary conditions. *NASA Tech. Rep.* NASA/TM-20220010483.
- MA, P.C., YANG, X.I.A. & IHME, M. 2018 Structure of wall-bounded flows at transcritical conditions. *Phys. Rev. Fluids* **3**, 034609.
- MITTAL, A. & GIRIMAJI, S.S. 2019 Mathematical framework for analysis of internal energy dynamics and spectral distribution in compressible turbulent flows. *Phys. Rev. Fluids* **4**, 042601(R).
- MODESTI, D. & PIROZZOLI, S. 2016 Reynolds and Mach number effects in compressible turbulent channel flow. *Intl J. Heat Fluid Flow* **59**, 33–49.
- MOIN, P. & MAHESH, K. 1998 Direct numerical simulation: a tool in turbulence research. *Annu. Rev. Fluid Mech.* **30** (1), 539–578.
- MORINISHI, Y., TAMANO, S. & NAKABAYASHI, K. 2003 A DNS algorithm using B-spline collocation method for compressible turbulent channel flow. *Comput. Fluids* **32** (5), 751–776.
- MORINISHI, Y., TAMANO, S. & NAKABAYASHI, K. 2004 Direct numerical simulation of compressible turbulent channel flow between adiabatic and isothermal walls. *J. Fluid Mech.* **502**, 273–308.
- MORKOVIN, M. 1962 *Effects of Compressibility on Turbulent Flows*. Centre National de la Recherche Scientifique.
- MOSER, R., KIM, J. & MANSOUR, N. 1999 Direct numerical simulation of turbulent channel flow up to $Re_\tau = 590$. *Phys. Fluids* **11** (4), 943–945.
- NAGATA, M. & NAGAOKA, M. 2017 Effects of strong temperature gradient on a compressible turbulent channel flow. In *Proceedings of the 10th International Symposium on Turbulence and Shear Flow Phenomena*, paper no. P-12.
- SERRA, S., TOUTANT, A., BATAILLE, F. & ZHOU, Y. 2012 High-temperature gradient effect on a turbulent channel flow using thermal large-eddy simulation in physical and spectral spaces. *J. Turbul.* **13** (49), N49.
- SHADLOO, M.S., HADJADI, A. & HUSSAIN, F. 2015 Statistical behavior of supersonic turbulent boundary layers with heat transfer at $M_\infty = 2$. *Intl J. Heat Fluid Flow* **53**, 113–134.
- SONG, Y.B., ZHANG, P., LIU, Y.L. & XIA, Z.H. 2022 Central mean temperature scaling in compressible turbulent channel flows with symmetric isothermal boundaries. *Phys. Rev. Fluids* **7**, 044606.
- SONG, Y.B., ZHANG, P. & XIA, Z.H. 2023 Predicting mean profiles in compressible turbulent channel and pipe flows. *Phys. Rev. Fluids* **8**, 034604.
- SPINA, E.F., SMITS, A. & ROBINSON, S.K. 1994 The physics of supersonic turbulent boundary layers. *Annu. Rev. Fluid Mech.* **26**, 287–319.
- SUN, D., GUO, Q.L., YUAN, X.X., ZHANG, H.Y., LI, C. & LIU, P.X. 2021 A decomposition formula for the wall heat flux of a compressible boundary layer. *Adv. Aerodyn.* **3**, 33.

DNS of compressible turbulent channel flows

- TAMANO, S. & MORINISHI, Y. 2006 Effect of different thermal wall boundary conditions on compressible turbulent channel flow at $M = 1.5$. *J. Fluid Mech.* **548**, 361–373.
- TANG, J., ZHAO, Z., WAN, Z.H. & LIU, N.S. 2020 On the near-wall structures and statistics of fluctuating pressure in compressible turbulent channel flows. *Phys. Fluids* **32** (11), 115121.
- TOKI, T., TERAMOTO, S. & OKAMOTO, K. 2020 Velocity and temperature profiles in turbulent channel flow at supercritical pressure. *J. Propul. Power* **36** (1), 3–13.
- TRETTEL, A. & LARSSON, J. 2016 Mean velocity scaling for compressible wall turbulence with heat transfer. *Phys. Fluids* **28** (2), 026102.
- VAN DRIEST, E.R. 1951 Turbulent boundary layer in compressible fluids. *J. Aero. Sci.* **18** (3), 145–160.
- VOLPIANI, P.S., IYER, P.S., PIROZZOLI, S. & LARSSON, J. 2020 Data-driven compressibility transformation for turbulent wall layers. *Phys. Rev. Fluids* **5** (5), 052602.
- WANG, W.P. & PLETCHER, R.H. 1996 On the large eddy simulation of a turbulent channel flow with significant heat transfer. *Phys. Fluids* **8** (12), 3354–3366.
- WEI, L. & POLLARD, A. 2011 Interactions among pressure, density, vorticity and their gradients in compressible turbulent channel flows. *J. Fluid Mech.* **673**, 1–18.
- WENZEL, C., GIBIS, T. & KLOKER, M. 2022 About the influences of compressibility, heat transfer and pressure gradients in compressible turbulent boundary layers. *J. Fluid Mech.* **930**, A1.
- XU, D.H., WANG, J.C. & CHEN, S.Y. 2022 Skin-friction and heat-transfer decompositions in hypersonic transitional and turbulent boundary layers. *J. Fluid Mech.* **941**, A4.
- XU, D.H., WANG, J.C., WAN, M.P., YU, C.P., LI, X.L. & CHEN, S.Y. 2021 Effect of wall temperature on the kinetic energy transfer in a hypersonic turbulent boundary layer. *J. Fluid Mech.* **929**, A33.
- YAO, J. & HUSSAIN, F. 2020 Turbulence statistics and coherent structures in compressible channel flow. *Phys. Rev. Fluids* **5**, 084603.
- YU, M., XU, C.X. & PIROZZOLI, S. 2019 Genuine compressibility effects in wall-bounded turbulence. *Phys. Rev. Fluids* **4**, 123402.
- ZHANG, P., SONG, Y.B., LIU, Y.L. & XIA, Z.H. 2022 Equivalence of three thermal boundary conditions in compressible turbulent channel flows. *Phys. Rev. E* **105** (14), 065106.
- ZHANG, P., SONG, Y.B. & XIA, Z.H. 2021 Exact mathematical formulas for wall-heat flux in compressible turbulent channel flows. *Acta Mech. Sin.* **38**, 321403.
- ZHANG, P. & XIA, Z.H. 2020 Contribution of viscous stress work to wall heat flux in compressible turbulent channel flows. *Phys. Rev. E* **102** (8), 043107.
- ZHANG, Y.S., BI, W.T., HUSSAIN, F. & SHE, Z.S. 2014 A generalized Reynolds analogy for compressible wall-bounded turbulent flows. *J. Fluid Mech.* **739**, 392–420.